MECHANICAL PROPERTIES OF $Sc_{0.1}Ce_{0.01}Zr_{0.89}O_2$ ELECTROLYTE MATERIAL FOR INTERMEDIATE TEMPERATURE SOLID OXIDE FUEL CELLS

A Thesis

by

WENDY LIM

Submitted to the Office of Graduate Studies of
Texas A&M University
in partial fulfillment of the requirements for the degree of

MASTER OF SCIENCE

December 2009

Major Subject: Mechanical Engineering

MECHANICAL PROPERTIES OF $Sc_{0.1}Ce_{0.01}Zr_{0.89}O_2$ ELECTROLYTE MATERIAL FOR INTERMEDIATE TEMPERATURE SOLID OXIDE FUEL CELLS

A Thesis

by

WENDY LIM

Submitted to the Office of Graduate Studies of
Texas A&M University
in partial fulfillment of the requirements for the degree of

MASTER OF SCIENCE

Approved by:

Chair of Committee,	Miladin Radovic
Committee Members,	Anastasia Muliana
	Haiyan Wang
Head of Department,	Dennis O'Neal

December 2009

Major Subject: Mechanical Engineering

ABSTRACT

Mechanical Properties of $Sc_{0.1}Ce_{0.01}Zr_{0.89}O_2$ Electrolyte Material for Intermediate Temperature Solid Oxide Fuel Cells. (December 2009)

Wendy Lim, B.S., The University of Texas at Austin

Chair of Advisory Committee: Dr. Miladin Radovic

Scandia doped zirconia has been considered a candidate for electrolyte material in intermediate temperature Solid Oxide Fuel Cells (SOFCs) due to its high ionic conductivity, chemical stability and good electrochemical performance. The aim of this study is to determine the mechanical properties of SCZ, ie. zirconia (ZrO_2) doped with Scandia (Sc_2O_3) and small amount of ceria (CeO_2) that are important for reliability and durability of the components manufactured from SCZ.

The SCZ was prepared from powder by uniaxiall cold pressing at subsequent sintering at 1550 ^{0}C for 4 hours. The density and porosity of the sintered samples was measured following the ASTM Standard C20-00 for alcohol immersion method. A pure cubic phase of SCZ sample was identified by X-ray diffraction (XRD) at room temperature. Quantitative compositional analyses for Zr, Sc, Ce, Hf and Ti were carried out on a Cameca SX50 electron microprobe with wavelength-dispersive spectroscopy (WDS) and energy-dispersive spectroscopy (EDS). Scanning Electron Microscopy (SEM) images were acquired using both secondary electron (SE) and back-scattered electron (BSE) detectors. WDS and EDS analysis also revealed that Zr, Sc, Ce, Hf and Ti are relatively homogeneously distributed in the structure. The average grain size of sintered SCZ samples was measured to be 4 μm.

Thermal expansion at different temperatures for the SCZ ceramic was determined using Thermal Mechanical Analyzer, and the instantaneous Coefficient of Thermal Expansion (CTE) was found to be 8.726×10^{-6} 1/^{o}C in the in 25-400 ^{o}C temperature range. CTE increases monotonically with temperature above 400 ^{o}C to

$1.16x10^{-5}$ at 890 ^{0}C, most likely as a result of thermo-chemical expansion due to an increase in oxygen vacancy concentration. Room temperature Vickers hardens of 12.5 GPa was measured at loads of 1000 g, while indentation fracture toughness was found to vary from 2.25 to 4.29 MPa $m^{1/2}$, depending on the methodology that was used to calculate fracture toughness from the length of the median corner cracks.

Elastic moduli, namely Young and shear moduli were determined using Resonance Ultrasound Spectroscopy (RUS). It was found that elastic moduli decreases with temperature in non-linear manner, with significant drop in the 300-600 ^{o}C temperature range, the same temperature range in which loss modulus determined by Dynamic Mechanical Analyzer exhibits frequency dependant peaks. The high loss modulus and significant drop in elastic moduli in that temperature regime is attributed to the relaxation of doping cation-oxygen vacancies clusters.

The flexural strength in 4-point bending was measured at room temperature, 400 ^{o}C, 600 ^{o}C and 800 ^{o}C. and the results were analyzed using Weibull statistics. It was found that flexural strength changes with temperature in a sigmoidal way, with the minimum strength at around 600 ^{o}C. Non-linear decrease in strength with temperature can be traced back to the changes in elastic moduli that are caused predominately by relaxation of oxygen vacancies.

DEDICATION

To my loving parents

ACKNOWLEDGEMENTS

I would like to express my deepest gratitude to the chair of my advisory committee, Dr. Miladin Radovic, for his guidance, encouragement and support throughout the course of my study at Texas A&M University. I also would like to thank my committee members, Dr. Anastasia Muliana and Dr. Haiyan Wang, for their assistance in my research.

I want to thank Dr. Nina Orlovskya from the University of Central Florida, Orlando, FL for providing samples for my research.

I would like to thank my fellow students, Patrick Mahaffey, Manisha, Kevin Flynn and Maricela Lizcano, for their help. Dr. Ray Guillemette is acknowledged for his help in Scanning Electron Microscopy (SEM). Special thanks also go to Ji Ma for his assistance in X-Ray Diffraction (XRD). Shreyas Balachandran is appreciated for his help in Microhardness Tester LM 300AT. My thanks also go to Patricia Alford for her help in providing reference services. I want to thank Jan Gerston, Dr. Sai Lau, Missy Cornett, Jim Sajewski, William Seward, Sheryl Mallett, Sarah Morgan, Dori Wilson and Casey Schumacher for their help.

I would like to thank my family and friends who have motivated and supported me throughout my studies.

NOMENCLATURE

TAMU	Texas A&M University
SOFCs	Solid Oxide Fuel Cells
WDS	Wavelength-Dispersive Spectrometers
SEM	Scanning Electron Microscopy
EDS	Energy-Dispersive Spectroscopy
BSE	Backscattering Electron
SE	Secondary Electron
TMA	Thermal Mechanical Analyzer
E	Young Modulus
G	Shear Modulus
ν	Poisson Ratio
K_{IC}	Fracture Toughness
HV	Vickers hardness number
XRD	X-Ray Diffraction Resonant
RUS	Resonant Ultrasound Spectroscopy
DMA	Dynamic Mechanical Analysis
CTE	Coefficient of Thermal Expansion
SCZ	Scandia and Ceria doped Zirconia
SDZ	Scandia Doped Zirconia
SZ	Stabilize Zirconia
ScSZ	Scandia Stabilized Zirconia
YSZ	Yttria Doped Zirconia
3Y-TZP	Tetragonal Zirconia Polycrystal
8YSZ	8 mol% Yttria Stabilized Zirconia
8Y-FSZ	8 mol% Yttria Doped Fully Stabilized Zirconia
DKKK	Daiichi Kigenso Kagaku Kogyo
MW	Molecular Weight

S	Strength
P_s	Probability of survival

TABLE OF CONTENTS

Page

LIST OF FIGURES

Page

Page

LIST OF TABLES

1. INTRODUCTION

1.1. Solid Oxide Fuel Cells

Fuel Cells offer high chemical to electrical conversion efficiencies and low emission of air pollutants such as NO_x and SO_x. Because of efficient energy conversion, high structural integrity and, reliability and nonpolluting service, Fuel Cells are used as energy sources in many applications ranging from small auxilary power unit to large scale power plants [1-6]. Moreover, they are used as alternative power generation systems to operate on natural gas, hydrogen, diesel, etc. due to their fuel flexibility [7-11].

Solid oxide fuel cells (SOFCs) are "ceramic fuel cells" based on ionic conducting electrolytes [12]. SOFCs operate in 600 – 1000 ^{0}C temperature range and use a solid electrolyte (such as doped zirconia, ceria, etc.). The output of SOFC can be up to 100 kW at the operating efficiency is about 60%. SOFCs are composed of an anode and cathode separated by solid electrolyte. The oxygen molecules from the air enter a fuel cell at the cathode and separate into oxygen ions with the addition of four electrons. During operation, a solid electrolyte conducts oxygen ions from the cathode to the anode and combines with hydrogen at the anode releasing four electrons. The electrons pass a circuit delivering electric power and **Figure 1.1** shows the operation of SOFC [13].

The electrochemical reactions in SOFC can be given as following [13]:

Anode Reaction: $2H_2 + 2O^{2-} \rightarrow 2H_2O + 4e^-$ ……..(1.1)

Cathode Reaction: $O_2 + 4e^- \rightarrow 2O^{2-}$ ……...(1.2)

Total Cell Reaction: $2H_2 + O_2 \rightarrow 2H_2O$ ……...….. (1.3)

This thesis follows the style of Solid State Ionics.

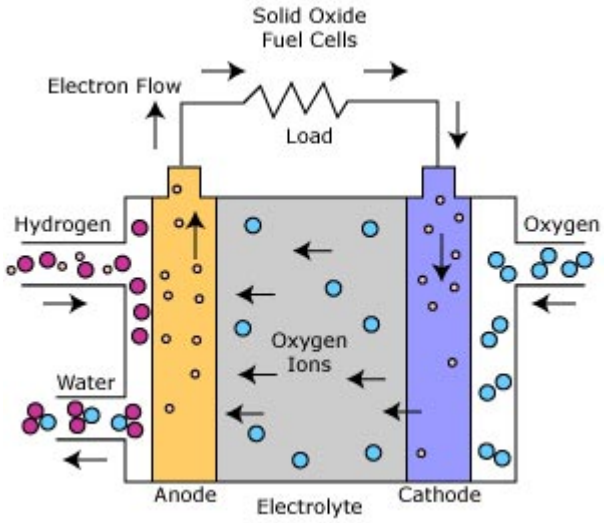

Figure 1.1 Operation concept of a SOFC [13]

The main components of SOFCs are electrolyte, cathode, anode and interconnect. The main requirements for electrolyte, anode, cathode and interconnect materials are discussed in more detail in the following paragraphs.

1.1.1. Electrolyte

The main purpose of SOFCs electrolyte is to conduct oxygen ions from cathode to anode. The key requirements for the solid electrolytes are summarized as follows:

- The electrolyte should have good ionic conduction to minimize cell impedance but with little or no electronic conductivity;
- The electrolyte should be chemically and mechanically compatible with other fuel cells components;
- The electrolyte should be structurally and dimensionally stable across a wide temperature range in fuel and oxidant environments;
- The electrolyte must have similar thermal expansion with other fuel cells components to minimize mechanical stresses during fabrication process and operation;
- Other requirements for SOFCs electrolyte are low cost, high strength and toughness.

Since early 1960s, large number of different fast ionic conductors such as ZrO_2, ThO_2, HfO_2, CeO_2, and δ-Bi_2O_3 has been used as electrolyte material in SOFC [14-18]. Nowadays, the most common electrolyte materials are Y_2O_3 and/or Sc_2O_3 stabilized ZrO_2 (YSZ or ScSZ), ceria compound, and Lanthanum-Gallates [19].

1.1.2. Cathode

The main purpose of SOFCs cathode is to reduce oxygen from air. Various requirements for the cathode materials are:

- The cathode should have good electronic conduction to carry the current flow and ionic conductivity to permit the transport of oxygen ions;
- The cathode should be chemically and mechanically compatible with other fuel cells components;
- The cathode should be structurally and dimensionally stable across a wide temperature range in oxidant environments;
- The cathode must have similar thermal expansion with other fuel cells components to minimize mechanical stresses during fabrication process and operation;
- The cathode must be porous to permit gas transport.
- The SOFCs cathode should be inexpensive material with high strength and toughness.

At the present time, Sr doped $LaMnO_3$, LSM and mixed ionic conductors such as La_1-xSr_xCo_1-yFe_yO_3, La_1-xSr_xFeO_3, La_1-xNi_xFeO_3 with Perovskite structure are commonly used as a cathode in SOFCs [19].

1.1.3. Anode

The main purpose of SOFCs anode is to oxidize fuel (H_2) and promote the sites for the fuel gas to react with the oxide ions. Different requirements for the anode materials can be summarized as following:

- The anode should have good ionic and electronic conduction to carry the current flow in the reducing environment;

- The anode should be chemically and mechanically compatible with other fuel cells components;
- The anode should be structurally and dimensionally stable across a wide temperature range in fuel environment;
- The anode must have similar thermal expansion with other fuel cells components to avoid cracking in the fabrication process and operation.
- The anode must be porous to permit transport of the fuel gas.
- Other requirements for SOFCs anode are low cost, high strength and toughness.

There are several ceramic-metal (cermet) composite materials such as Ni-YSZ, Ni-Ce-YSZ, and Ni-ScSZ [19] that are commonly used at the present time as an anode materials for SOFC.

1.1.4. Interconnect

The main purpose of SOFCs interconnect is to transport the electrical current from the electrochemical cell to the external circuit. They also serve as a manifold for fuel and oxidizing gases. The key requirements for the interconnect materials are:

- An interconnect should have good electronic conduction to carry electrons from anode to cathode;
- An interconnect should be chemically and mechanically compatible with other fuel cells components;
- An interconnect should be structurally and dimensionally stable across a wide temperature range in reducing (fuel) and oxidizing (oxidant) environments;
- An interconnect must have similar thermal expansion with other fuel cells components to avoid cracking in the fabrication process and operation.
- An interconnect should be fully dense to prevent gas cross leakage.
- Other requirements for SOFCs interconnect are low cost, high strength and toughness.

The $LaCrO_3$, chromite ceramic and chromium based metallic alloys are considered to be the best interconnect in SOFCs at the present moment.

The main advantage of SOFCs compared to other power conversion devices is that SOFCs transform chemical energy to electricity at high efficiency (45-65%) because their efficiencies are not limited by the Carnot cycle. In addition, SOFCs offer high waste heat for cogeneration systems and have high tolerance for different fuels. SOFCs operation at high temperatures permits internal reformation of different fuels such as natural gas, gasoline, diesel, etc. They are environmentally friendly because of low emission level and silent generation of electricity. The material costs for SOFCs are lower when compared to other fuel cells because they do not require use of expensive catalysts.

However, the major disadvantages of SOFCs are related to relatively high operating temperatures that requires slow startups times. Since they consist of dissimilar ceramic materials, temperature gradients during transient and service regime can generate large thermal stresses that can limit reliability and durability of SOFCs.

Although SOFC are highly-efficient and environmentally friendly electrochemical devices that convert the chemical energy of fuel directly into electrical energy [20, 21], their reliability depends not only on the chemical and electrochemical stability of its components but also on the capability of the SOFC components to withstand mechanical stresses that arise during processing and service. In the case of SOFC, the mechanical reliability and durability is determined by the stress distribution in, and the stochastic distribution of, strengths of its components [22]. The stress distribution is a complex function of several parameters including geometry of the fuel cell, temperature distribution, properties of the constitutive materials (coefficient of thermal expansion and elastic moduli) and external mechanical loads [23-26]. Furthermore, residual stresses are introduced during processing as a result of mismatch in the thermo-elastic properties and shrinkage during sintering of fuel cell components [27-30]. Since hydrogen is supplied on the anode side of the SOFC stack and oxygen on the cathode side, the oxygen potential gradient and thus the different concentration of the point defect is present across the electrolyte in an SOFC stack [31]. Recently, Swaminathan et. al. [32] and Krishnamurthy et al. [33] showed that significant chemical

stresses (up to 500 MPa) can develop in SOFC electrolyte due to oxygen potential gradients. Stresses developed in SOFC components also affect diffusion and transport properties of constituent materials, and thus electrochemical performance of the SOFC [34-37]. For example, Araki et al. [38] reported increase in ionic conductivity of typical SOFC electrolyte material (zirconia stabilized with 8 mol% yttrium) up to 18% when it is exposed to tensile stresses at elevated temperatures.

Therefore, in order to develop more reliable and durable components for SOFC oxide ceramics, it is necessary to understand the mechanical properties of SOFC's materials at different temperatures. A high strength and tough materials for SOFC with similar thermal expansions are very desirable for increasing reliability and durability of SOFCs because:

- they will minimize the stresses that generated during processing and service; and
- they are less responsive to the presence of flaws introduced during the fabrication and/or service.

1.2. Zirconia as Solid Electrolytes

Stabilized (cubic) Zirconia based electrolyte is used as a solid electrolyte in SOFCs because it exhibit high ionic conductivity at elevated temperatures. The conductivity of the zirconia based electrolyte is heavily dependent on the service temperature of SOFCs. Cubic Zirconia has fluorite structure at 2370 ^{0}C which can be stabilized even at room temperature by doping with lower valent oxides such as CaO, Y_2O_3, or Sc_2O_3 [12]. The fluorite structure (**Figure 1.2**) is a face-centered cubic lattice with anions occupies all the tetrahedral sites.

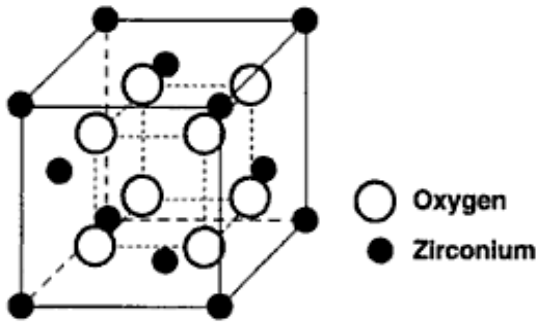

Figure 1.2 Cubic structure of Zirconia

It is important to stabilize cubic structure of Zirconia for SOFC's electrolyte within the entire operating temperature range from room temperature to 1000 ^{0}C to avoid abrupt decrease in oxygen ion conduction during cooling due to the instability of cubic phase at lower temperatures [14-18, 39]. However, even for fully stabilized cubic structures, aging effects in SOFC systems at high temperature (700-1000 ^{0}C) can result in the local ordering toward the formation of tetragonal structure in the cubic matrix [40].

The addition of divalent or trivalent dopant not only stabilizes cubic structure at room temperature, but also assists in increasing the concentration of oxygen vacancies, and thus, the ionic conductivity [41, 42] of zirconia. For example, Y_2O_3 stabilized cubic zirconias (YSZ) is one of the most popular solid electrolyte materials nowadays that is widely used in oxygen sensors and SOFCs [43]. Doping ZrO_2 with Y_2O_3 results in formation of mobile oxygen vacancies, according to the following chemical reaction [44]:

$$Y_2O_3(ZrO_2) \rightarrow 2Y'_{Zr} + V''_O + 3O_O \quad \text{.....(1.4)}$$

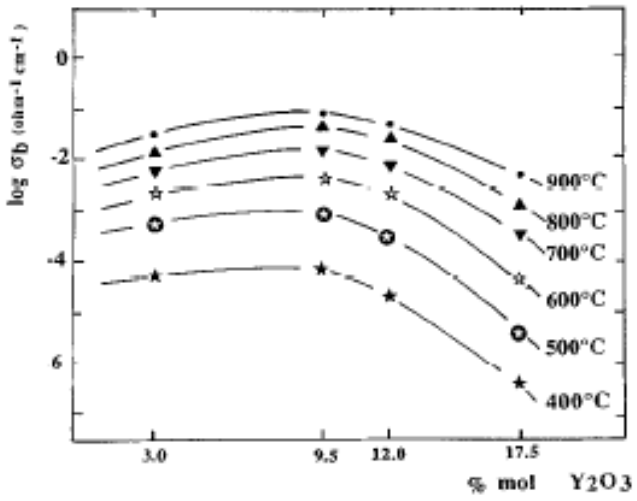

Figure 1.3 Influence of the amount of Y_2O_3 on the ionic conductivity of zirconia single crystals [45]

According to Eq. 1.4 one oxygen vacancy is produced for every two Y ions replacing two Zr ions. Thus, addition of dopant increases concentration of oxygen vacancies and diffusivity of oxygen ions and ionic conductivity. It was shown that the ionic conductivity of zirconia increases significantly for increasing yttria content up to concentration of 9-10 mol% yttria, **Figure 1.3**. A maximum ionic conductivity of zirconia is reached in the 9.5 mol% Y_2O_3 (independent of temperature). The ionic conductivity decrease after 9.5 mol% Y_2O_3 is a result of the formation of dopant vacancy associations over the whole temperature range. The appearance of a maximum in the oxygen ion conductivity of Y_2O_3 stabilized ZrO_2, **Figure 1.3**, is related to increase in oxygen vacancy concretion that becomes entrapped by doping cations at concentrations above approximately 9-10 mol%. In other words, as the dopant concentration increases, the distorted region decreases in size, and the disorder becomes dominated by formation of vacancy-dopant (cation) clusters.

The decrease in conductivity at higher dopant concentration is thus result of defect ordering, vacancy clustering, or electrostatic interaction [46, 47]. To obtain the significant increase in ionic conductivity, the zirconium ions (the ionic radius of 0.082 nm) has to be substituted by a cation with a more similar ionic radius, so that lattice

strain are minimized and fewer oxygen ion vacancy are association with the doping cations.

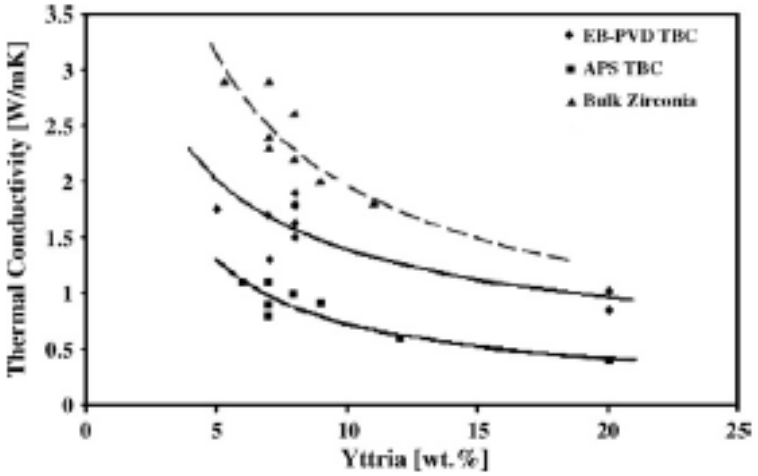

Figure 1.4 Thermal conductivities of zirconia ceramic and coatings vs. yttria content [45, 48]

Apart from ionic conductivity and diffusivity, the defect structure will determine the mechanical and thermal properties of cubic, stabilized zirconia [38, 49-51]. For example, the thermal conductivity of zirconia decreases initially as the yttria contents increases (**Figure 1.4**).

It is very important to improve the mechanical properties of cubic zirconia because the strength and fracture toughness are usually not sufficiently high to use YSZ as electrolyte material for SOFC. It has been reported by Wiedenmann et. al. [52] that the doping zirconia with yttria provides not only high ionic conductivity, but also high mechanical strength. The ionic conductivity and mechanical properties of zirconia rely on the yttria dopant content [53-55]. **Figure 1.3** highlight influence of the amount of Y_2O_3 on the ionic conductivity of zirconia mentioned earlier in this work [56, 57]. Pure zirconia can be stabilized in tetragonal phase at room temperature by the addition of only 2-2.5 mol% yttria [58]. Tetragonal phase has excellent mechanical properties. High mechanical strength of 1 GPa and high fracture toughness of 10 MPa $m^{1/2}$ is reported for tetragonal zirconia polycrystal (3Y-TZP) with 3 mol% of yttria at room temperature [54,

55, 59]. However, the ionic conductivity of 3 mol% Yttria doped Zirconia is relatively low. As a compromise, the yttria content is adjusted to 4-6 mol% yttria for high ionic conductivity and mechanical strength [60] in an exhaust gas sensor. Good mechanical properties of partially stabilized zirconia are attributed to presence of the tetragonal phase that converts into monoclinic phase accompanied by a volume expansion under mechanical stress. This guides to transformation toughening of zirconia producing not only high toughness, but also high strength of the material [61, 62].

In SOFC, zirconia doped with 8 mol% yttria is desirable as solid electrolyte because of its high ionic conductivity. At 8 mol% of yttria cubic phase is fully stabilized even at room temperature [53] and thus transformation toughening cannot be employed to improve mechanical properties [63]. To improve the mechanical properties of 8 mol% yttria stabilized zirconia (8YSZ), alumina [64, 65], neodymium titanate [66], $BaTiO_3$ [67], and monoclinic zirconia [68] were added as second phases in previous studies. M. Mori et al. [65] have showed the 3-point bending strength of 8YSZ and the composites at different temperature (**Figure 1.5**). At high temperature, the mechanical properties of 8YSZ were improved by addition of Al_2O_3 because the bending strength of alumina does not decrease with increasing temperatures.

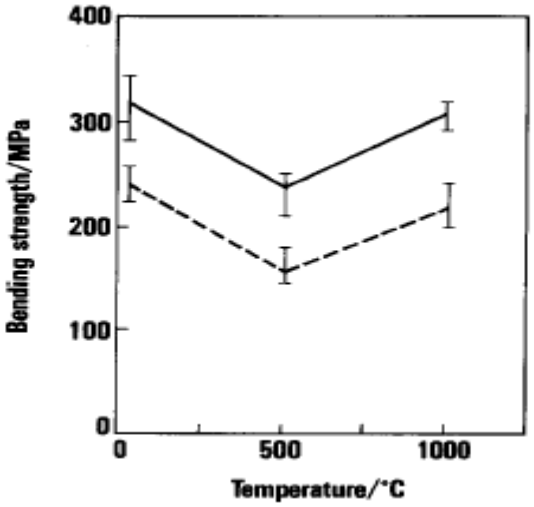

Figure 1.5 3-point bending strength of 20A8YSZ (—) and 8YSZ (---) at different temperature [65]

Xiao Qiang Liu and Xiang Ming Chen [66] have reported on the mechanical properties of 8 mol% yttria doped fully stabilized zirconia (8Y-FSZ). The grain size of ceramics increased by addition of small amount of $Nd_2Ti_2O_7$, but then decreased again with adding of larger amount of $Nd_2Ti_2O_7$ as shown in **Table 1.1**. A very high relative density was also attained with the addition of $Nd_2Ti_2O_7$. The hardness decreased at x = 0.25, but it was constant with varying $Nd_2Ti_2O_7$ content. The fracture toughness improved originally for low $Nd_2Ti_2O_7$ content, but then decreased as the $Nd_2Ti_2O_7$ content increased.

Table 1.1 Mechanical properties of $xNd_2Ti_2O_7/(1-x)8Y$-FSZ ceramics [66]

x	RD (%)	Grain size (μm)	H_v (GPa)	K_{IC} (MPa·$m^{1/2}$)
0.00	0.86	1.58	–	–
0.05	0.98	32.0	11.3±0.2	3.4±0.2
0.10	0.99	10.9	11.3±0.3	4.0±0.3
0.15	0.97	8.08	11.3±0.2	8.0±0.8
0.20	0.96	2.82	11.3±0.2	5.4±0.8
0.25	0.95	2.18	10.4±0.2	5.2±0.5
0.00†	0.91	–	8.9±2.8	3.2±0.3

X.Q. Liu and X.M. Chen [67] have reviewed microstructures and mechanical properties of 8Y-FSZ with $BaTiO_3$ additive. The $BaTiO_3$ phase can increase the grain size and density of 8Y-FSZ ceramics. The mechanical properties of $xBaTiO_3/(1-x)8Y$-FSZ ceramics under different sintering conditions are shown in **Table 1.2**. They concluded that the decrease in the Young's modulus of $xBaTiO_3/(1-x)8Y$-FSZ for high content of additive is due to a low modulus of $BaTiO_3$ phase. The hardness increases initially, but then decreases with increasing the additive content.

Table 1.2 Mechanical properties of $xBaTiO_3/(1-x)8Y$-FSZ ceramics under different sintering conditions [67]

Sintering conditions (°C/3 h)	Composition (x)	Density (g/cm^3)	Young's modulus (GPa)	Vickers hardness (GPa)	Fracture toughness ($MPa\,m^{1/2}$)
1450	0.05	5.74	133 ± 15	11.6 ± 0.3	4.4 ± 0.5
	0.10	5.74	159 ± 34	11.5 ± 0.3	4.1 ± 0.1
	0.15	5.51	185 ± 45	6.9 ± 0.1	3.8 ± 0.2
1475	0.05	5.70	176 ± 45	11.6 ± 0.8	6.1 ± 0.3
	0.10	5.63	167 ± 24	12.1 ± 0.3	4.6 ± 0.2
1500	0.05	5.68	154 ± 28	10.7 ± 0.9	5.0 ± 0.6
	0.10	5.58	147 ± 47	10.0 ± 0.2	4.6 ± 0.6
1525	0.05	5.62	143 ± 18	11.9 ± 0.3	5.2 ± 0.8
	0.10	5.50	134 ± 18	11.0 ± 0.6	4.6 ± 0.5
	0.15	5.24	115 ± 18	9.9 ± 1.5	3.6 ± 0.2
1550	0.05	5.63	131 ± 48	11.1 ± 0.6	4.7 ± 0.8
	0.10	5.52	128 ± 22	8.7 ± 0.2	4.0 ± 0.5
	0.15	5.27	90 ± 16	8.4 ± 0.1	3.8 ± 0.6
1600	0.00	5.36	149 ± 30	8.9 ± 2.8	3.2 ± 0.3

Fracture toughness of $xBaTiO_3/(1-x)8Y$-FSZ ceramics under different sintering conditions is shown on **Figure 1.6**. The fracture toughness increase of 8Y-FSZ ceramics is a result of the incorporation of $BaTiO_3$ additive. After the material reaches a maximum of 6.1 MPa $m^{1/2}$ at x = 0.05, the fracture toughness of the material begins to decrease.

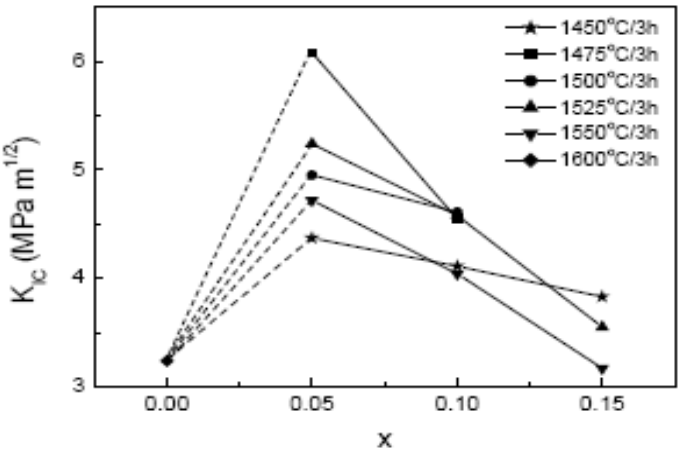

Figure 1.6 Fracture toughness of $xBaTiO_3/(1-x)8Y$-FSZ ceramics under different sintering conditions [67]

At high service temperatures of SOFC, the solid YSZ electrolyte degrades during service as a result of aging. For example, the decrease of ionic conductivity as a result of aging due to phase transitions in cubic zirconia, and cracking after extended service was reported in literature [40, 69, 70]. In order to prevent aging of zirconia based electrolyte and cracking that is caused by high thermal stresses due to the mismatch in thermal expansions of different materials in SOFC, the service temperature of SOFCs has to be lowered. Thus, there have been significant efforts over the last several years in reducing service temperatures of SOFC that in turn calls for new electrolyte materials that provide high ionic conductivities temperatures well below ~ 800 ^{0}C.

1.3 Scandia Doped Zirconia

Scandia doped Zirconia (SDZ) has been considered as a good candidate material for electrolyte in intermediate temperature SOFC due to its high ionic conductivity [42, 71]. **Figure 1.7** compares the ionic conductivity of different solid electrolyte materials at different temperatures [65, 72-78].

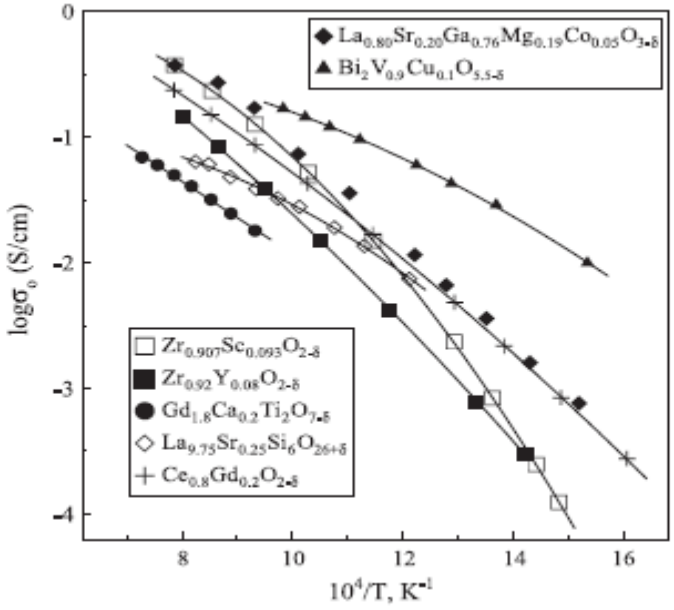

Figure 1.7 Oxygen ionic conductivity of different solid electrolyte materials at different temperatures [65, 72-78]

SDZ has higher ionic conductivity than YSZ because the ionic radius of the scandium (0.084 nm) is closer to the ionic radius of the zirconium (0.082 nm) and thus, the deformation of the crystal lattice by substituting zirconium cation with scandium cation is rather low [79-82]. It has been shown that as difference in size of the ionic radius between the Zr^{4+} ion and dopant ion decreases, the ionic conductivity increases (**Figure 1.8**) [83, 84].

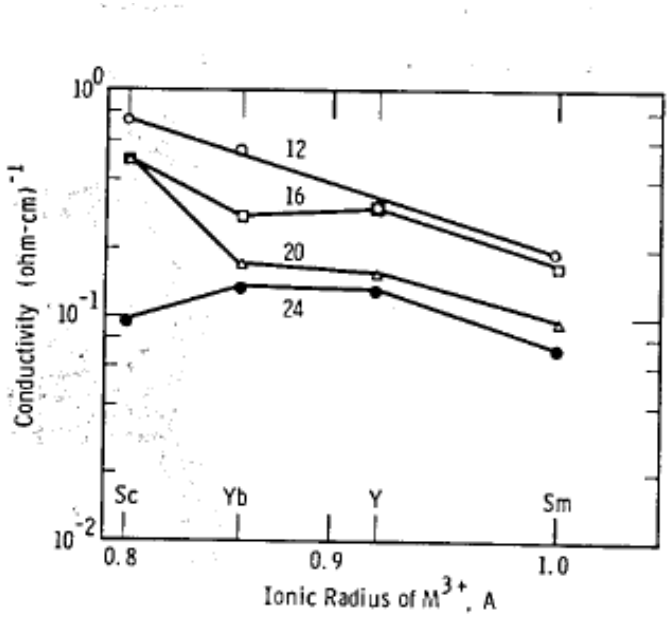

Figure 1.8 Oxygen ionic conductivity (1300 ^{0}C) vs. ionic radius for M_2O_3-ZrO_2 [84]. 12, 16, 20, 24 are different M_2O_3-ZrO_2 compositions

This is explained by decrease in activation energy of mobile oxygen ions with decreasing the difference between Zr^{4+} cation and dopant cation [84]. Thus, SDZ exhibits the highest value of electrical conductivity due to low enthalpy of defects reactions and the similarity between Sc^{3+} and Zr^{4+} ionic radii [85]. The ionic conductivity of SDZ decreases rapidly below 800 ^{0}C [86-88] but at 780 ^{0}C, the ionic conductivity of SDZ is comparable to that of YSZ at 1000 ^{0}C [89]. This offers significant lowering of service temperature of SOFC by using SDZ electrolyte instead of YSZ without sacrificing performance of the SOFC.

However, ZrO_2 doped with 8 mol% Sc_2O_3 shows significant aging after annealing at 1000 ^{0}C [90] and degradation of electrical conductivity [91]. The formation of rhombohedral phase that occurs during annealing process is found to be responsible for observed decrease in ionic conductivity [67]. Scandia doped zirconias have complex phase transformations in the temperature range that corresponds to the service temperatures of SOFCs. **Figure 1.9** provides a comprehensive summary phase changes in the ZrO_2-Sc_2O_3 systems [18]. The phase diagram indicates that there is a phase transition at 650 ^{0}C from cubic to rhombohedral phase for zirconia doped with ~10-13 mol% Sc_2O_3. This phase transition can lead to an abrupt change in volume and coefficient of thermal expansion (CTE) and thus cracking of the electrolyte material. The phase transition can be avoided by doping SDZ with a small amount of Al_2O_3 [39, 92] or CeO_2. It was reported that Zirconia was stabilized with CeO_2 and Sc_2O_3 did not demonstrate phase transition in intermediate temperature SOFC [93, 94]. D.-S. Lee et al. demonstrated that the cubic structure was stable in the 27-1550 ^{0}C temperature range [70]. It was reported that doping with CeO_2 also plays an important role in the increase of electrical conductivity at temperature of 300-1100 ^{0}C [70, 71]. Doping of scandia stabilized zirconia (ScSZ) with a small amount of oxides [17, 85, 89, 95-100] such as CeO_2, TiO_2, Bi_2O_3, Al_2O_3, Y_2O_3, increases not only stability of cubic structure but also electrical conductivity. Moreover Zirconia based fluorite structures was doped with a number of additives, such as CeO_2, Er_2O_3, Yb_2O_3, Y_2O_3, Sc_2O_3, or their mixture, in order to sustain oxygen conductivity at decrease temperature, but at the same time to stabilize the cubic ZrO_2 phase [99, 101-104].

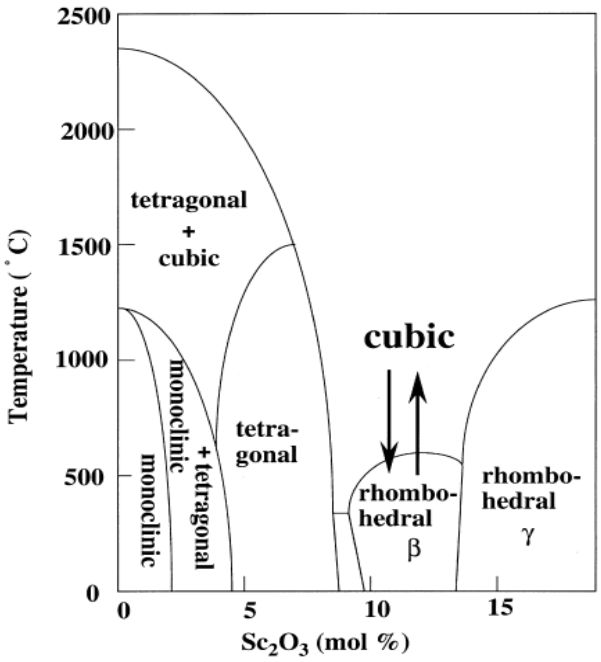

Figure 1.9 Phase diagram of the ZrO2-Sc2O3 system [18]

SDZ has good mechanical strength that it is comparable to that of yttria doped zirconia (YSZ) [45, 79, 105-107]. It is shown in **Table 1.3**.

Table 1.3 Electrical conductivity of Zirconia [106]

Electrolyte [a]	Conductivity (S/cm) at 1000°C	at 800°C		Bending strength (MPa)	Thermal expan. coeff. ($1/K \times 10^4$)	Ref.
	as sintered	after aging [b]	as sintered			
3Y-TZP	0.056	0.050	0.018	1200	10.8	[15]
8YSZ	0.13	0.09	0.03	230	10.5	[16]
9YSZ	0.13	0.12				[16]
3Yb-TZP	0.063	0.04	0.014			[15]
8YbSZ	0.20	0.15	0.063			
10YbSZ	0.15	0.15				
12YbSZ	0.10		0.02			
2.9Sc-TZP	0.09	0.063	0.031			
8ScSZ	0.30	0.012	0.13	275	10.7	
11ScZ	0.03	0.30	0.12			
12ScSZ	0.26	0.29	0.12	255		

[a] 3Y–TZP:3 mol% Y_2O_3–ZrO_2, 2.9 Sc–TZP: 2.9 mol% Sc_2O3–ZrO_2.
[b] After aging at 1000°C for 1000 h.

It has been shown that the amount addition of 3.5 mol% scandia results in the mechanical strength comparable to 2.5 mol% yttria [108-111]. Sc_2O_3 content with 3.5 mol% HIP at 1450 ^{0}C possessed the highest average strength of 1770 MPa and fracture toughness of 5.7 MPa $m^{1/2}$ [111]. It is shown in **Figures 1.10** and **1.11.**

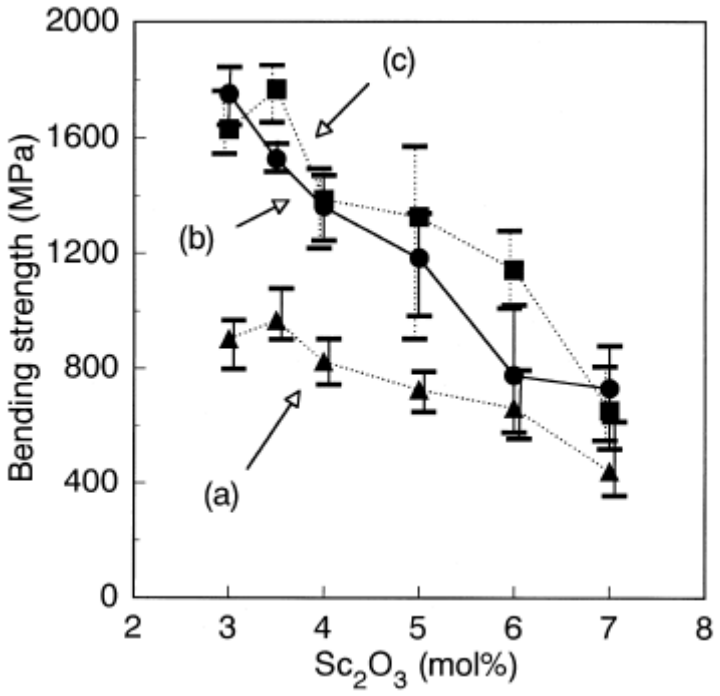

Figure 1.10 Bending strength of Sc_2O_3 doped zirconia (a) sintered at 1300 ^{0}C (b) HIP at 1300 ^{0}C (c) HIP at 1450 ^{0}C [111]

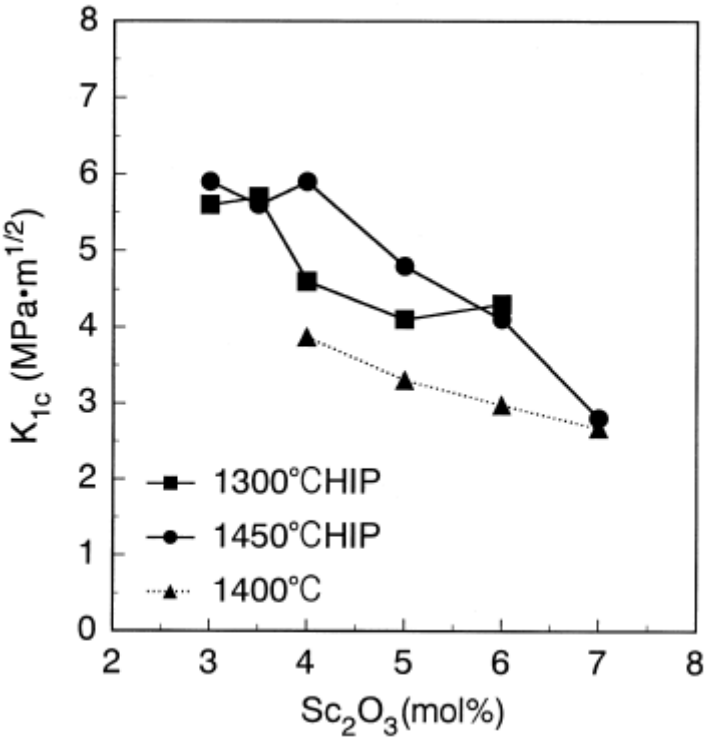

Figure 1.11 Fracture toughness of Sc_2O_3 doped zirconia sintered at 1400 ^{0}C [112], and HIP at 1300 and 1450 ^{0}C [111]

Figures 1.12 and 1.13 shows changes in the oxygen ionic conductivity and bending strength with amount of scandia, x, in $(Y_{0.148-x}Sc_x)Zr_{0.852}O_{1.925}$. It was found that as amount of doping scandia increases, ionic conductivity also increases while bending strength shows maximum at x=0.1.

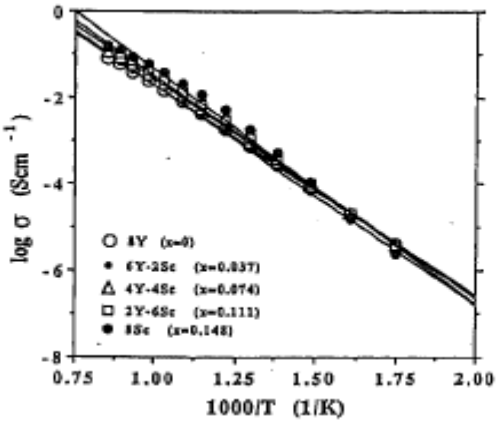

Figure 1.12 The oxygen ionic conductivity of $(Y_{0.148-x}Sc_x)Zr_{0.852}O_{1.925}$ [113]

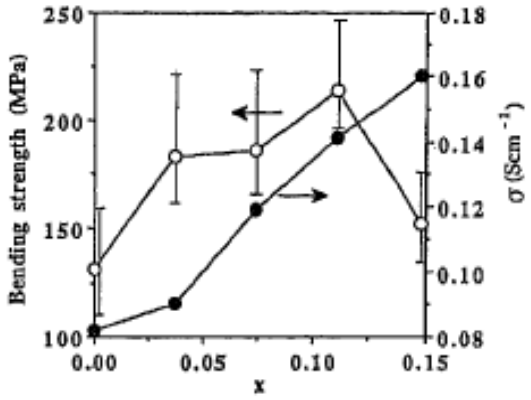

Figure 1.13 The bending strength (room temperature) and oxygen ionic conductivity (900 ^{0}C) in $(Y_{0.148-x}Sc_x)Zr_{0.852}O_{1.925}$ [113]

2. EXPERIMENTAL METHODS

2.1. Materials

The $ScCeZrO_2$ (SCZ) samples with true chemical composition of 9.51 mol% Sc_2O_3 + 1.49 mol% HfO_2 + 1.21 mol% CeO_2 + 87.07 mol% ZrO_2 where prepared from powder supplied by Daiichi Kigenso Kagaku Kogyo (DKKK), Japan [114]. The powder was cold pressed in disc shaped pellets or rectangular bars using uniaxial loads of 20 MPa. The green samples were sintered at 1550 ^{0}C in air for 4 hours, using heating and cooling rates of 5 ^{0}C/min.

2.2. Experimental Procedures

2.2.1 Density Measurements

The density of the sintered samples was measured following the ASTM Standard C20-00 for alcohol immersion method [115]. Analytical balance with resolution up to 0.0001g was used to measure the weight of the samples. First, the dry weight of the sample (W_{dry}) was measured and the samples were immersed in alcohol and kept in vacuum for 5 minutes. Then the immersed samples were removed from the vacuum and kept approximately 30 minutes at room temperature. After that, the temperature of alcohol was measured and the corresponding density for alcohol, $\rho_{alcohol}$ was determined from standard temperature-density tables (not shown here) for 200% proof ethyl alcohol. In the specimen suspension system, the wire basket was attached to the balance and immersed in the dish with alcohol and samples. The weight of suspended wire basket was recorded as $W_{wire.}$ Next, the sample was placed in the wire basket and suspended weight of the W_{Susp} was measured. Then, the sample was removed from alcohol and blotted with a tissue paper for 60 seconds to remove residue of alcohol on the surfaces.

After this process, the weight of the sample was measured and recorded as W_{Wet}. The bulk density, % open porosity, and % closed porosity are calculated as follows:

$$\text{Bulk Density}=W_{dry}\text{x}\frac{\rho_{Alcohol}}{(W_{Wet}-W_{Susp}+W_{Wire})} \quad \text{.....(2.1)}$$

$$\%\ \text{Open Porosity}=\frac{(W_{Wet}-W_{Dry})\text{X}100}{(W_{Wet}-W_{Susp}+W_{Wire})} \quad \text{.....(2.2)}$$

$$\%\ \text{Closed Porosity}=\left(\frac{W_{Wire}-W_{Dry}-W_{Susp}}{\rho_{Alcohol}}-\frac{W_{Dry}}{\rho_{Theoritical}}\right)\text{X}\left(\frac{100\text{X}\rho_{Alcohol}}{W_{Wire}-W_{Wet}-W_{Susp}}\right) \quad \text{.....(2.3)}$$

where $\rho_{alcohol}$ and $\rho_{Theoretical}$ are densities of 200% proof ethyl alcohol and theoretical density of SCZ, respectively. The theoretical density of 5.74 g/cm^3 SCZ is used to calculate closed porosity of samples, Eq. 2.3.

2.2.2 Optical Microscopy and Grain Size Measurements

The grain size measurements of SCZ ceramic were carrying out using Digital Microscope VHX-600 (Keyence, Japan). The examined samples were ground and polished using automatic polisher Ecomet 3 (Buehler, IL) at 170 rpm speed and 6 lbs force for 8 minute for each grit of sand paper. A grit of 320, 400, 600, 2400 and 4000 sand papers with water were initially used in a grinding process. After that, samples were polished using 3μm, 1μm, 0.5μm diamond suspension and toluene solvents at 170 rpm speed and 6 lbs force. To expose grains on the polished surface of SCZ sample, the sample was thermally etched. Thermal etching procedure involved heating to the temperature of 1500 ^{0}C, with a heating ramp rate of 5 ^{0}C/min and isothermal holding for 5 hours. After that, the sample was cooled to temperature from 1500 ^{0}C to 25 ^{0}C, with a

cooling rate of 5 ^{0}C/min. In this study, the air was used as a purge gas. **Figure 2.1** shows the surface of SCZ after polishing and thermal etching.

The polished and etched sample in the form of disc was placed on stage of Digital Microscope VHX-600, **Figure 2.2**. Average grain size was measured using linear intercept method. The length of each grain is measured along the line and these length measurements were used to calculate the average and standard deviation of grain size. The size, or intercept length of total 111 grains was measured.

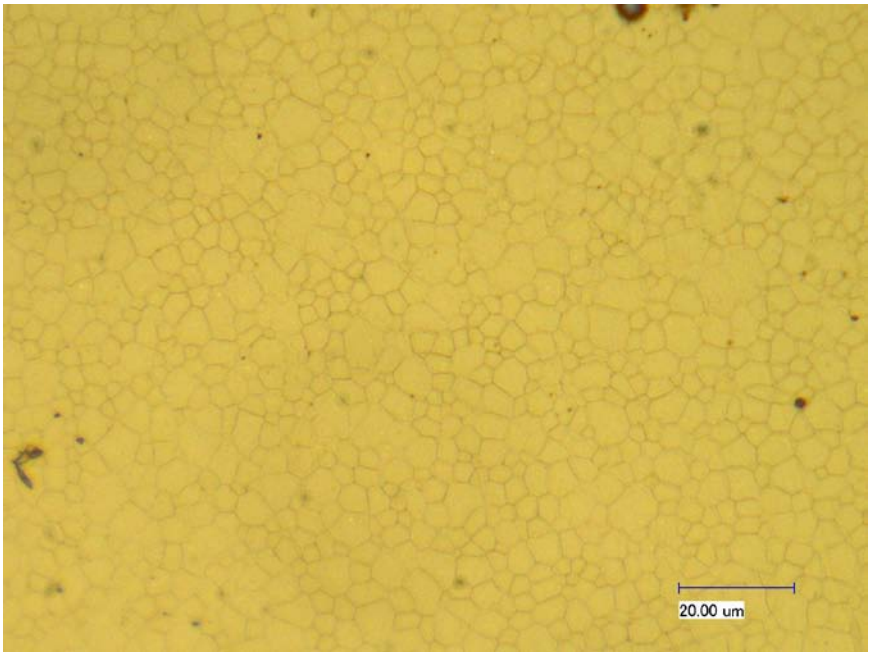

Figure 2.1 Sintered surface of SCZ

Figure 2.2 Digital Microscope VHX-600

2.2.3 Scanning Electron Microscopy (SEM)

Compositional analyses for Zr, Sc, Ce, Hf and Ti in SCZ were carried out using Cameca SX50 electron microprobe, ie. Scanning Electron Microscope (SEM) equipped with Energy-Dispersive Spectrometer (EDS) and Wavelength-Dispersive Spectrometer (WDS). A WDS spectrometer is a monochromator which consists of a rotatable, oriented diffraction crystal coupled with a proportional gas-filled ionization detector in a geometric relationship following Bragg's Law. WDS was used for compositional study rather than EDS because the former has better resolution, detection limits, accuracy and reproducibility. Analyses were carried out at an accelerating voltage of 15 KV at a beam current of 50 nA. The following standards were used: $ZrSiO_4$ for Zr, $ScPO_4$ for Sc, $CePO_4$ for Ce, Hf metal for Hf, and TiO_2 for Ti. All analyses were processed using the Cameca PAP (Pouchot and Pichoir) full-quantitative matrix correction program. **Figure 2.3** shows a Cameca SX50 electron microprobe while **Figure 2.4** shows a schematic of Cameca SX50 electron microprobe.

Figure 2.3 A Cameca SX50 electron microprobe [116]

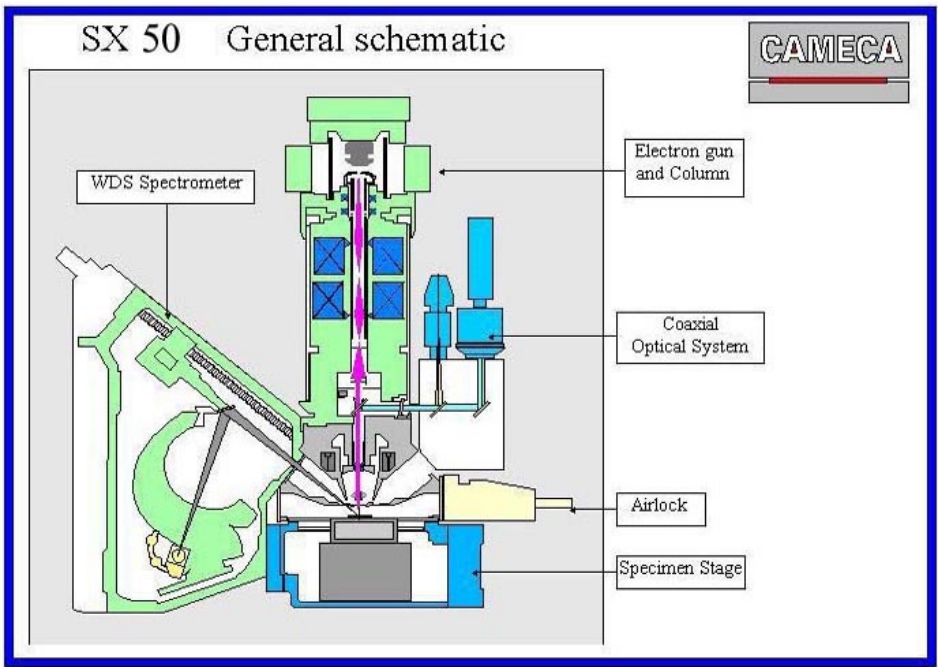

Figure 2.4 A detailed view of Cameca SX50 electron microprobe [116]

The SEM images were acquired using both Secondary Electron (SE) and Back-Scattered Electron (BSE) detectors to analyze phase distribution of the sample. SE imaging using low-energy electrons emitted from near the surface; this emphasizes topography (shape) of the surface. BSE imaging relies on high energy, elastically rebounding electrons; on polished surfaces, this allows to observe differences in mean atomic number as differences in brightness, allowing grains of different composition to be distinguished. Qualitative X-ray spectra were obtained using the PGT Imix EDS system on the SX50.

Samples were coated with 15nm thick layer of spectroscopically pure carbon in a Ladd carbon evaporator, **Figure 2.5,** prior to analysis in order to prevent electrical charging of the specimen surface under the electron beam. Samples were secured to the sample stage with conductive double-sided carbon tape.

Figure 2.5 A Ladd carbon evaporator [116]

2.2.4 X-ray Diffraction (XRD)

The crystal structure of SCZ ceramic (polycrystalline material) was determined using Bruker AXS D8 Discover X-Ray Diffractometer. XRD analysis was performed at room temperature in air on the polished, un-etched, surfaces of SCZ sample. **Figure 2.6** illustrates the basic operational principle of XRD technique. The polished surface sample was placed on stage and rotated to change the angle of the incident X-ray beam. A detector was used to measure intensity of X-ray peak as a function of the 2θ angle. An X-ray beam diffracts of the planes in a crystal lattice that were separated from each other by a distance d and results in the peak in diffraction spectra when wavelength, λ, distance between planes, d, and incident angle θ, satisfy following equation:

$n\lambda = 2d \sin \theta$……..……(2.4)

where n is integer number, ie. n=1,2,3,….Equation 2.4 is known as Bragg's Law and it allows us to calculate distance between different planes in crystal structure, and thus determine crystal structure of the sample and lattice parameters.

XRD experiment was performed at voltage of 40 kV and amperage of 40 mA. The scan of 2θ was carried out in 20^{0} to 80^{0} 2θ range at the speed of 0.1 second/step and increments of 0.02^{0}. After initial XRD peaks were detected, Z scan was carried out to get highest peak/intensity. A 4 hours final scan in 20^{0} – 120^{0} 2θ range was used to obtain more accurate XRD patterns and less noise at the speed of 3 second/step and increments of 0.02^{0}. Figure 2-7 shows Bruker AXS D8 Discover X-Ray Diffractometer that was used in this work.

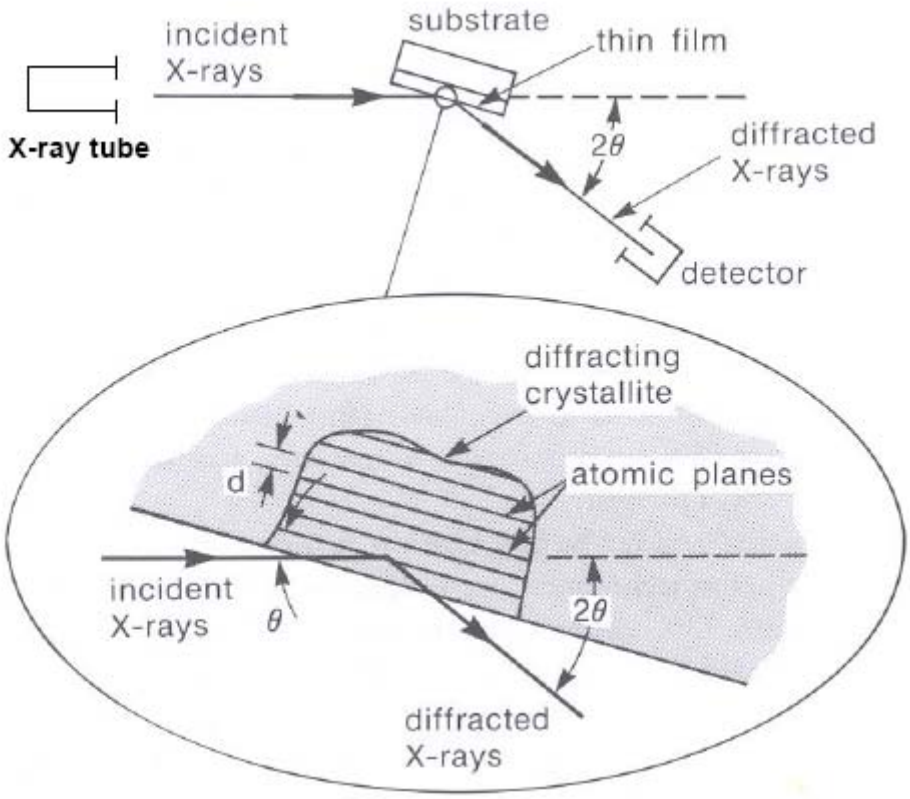

Figure 2.6 Typical XRD experiment [117]

Figure 2.7 Bruker AXS D8 Discover X-Ray Diffractometer

2.2.5 Thermo Mechanical Analysis

Thermal expansion of SCZ ceramic was measured using Q400 series Thermal Mechanical Analyzer (TMA), TA Instruments, IL, USA that is shown in **Figure 2.8**. The 5x4x8 mm sample was machined by BOMAS, Inc., Somerville, MA, to achieve the smooth and parallel surfaces. The sample dimensions were selected to meet recommendations of instrument manufacturer. The mass of the sample was measured before and after the test to observe eventual change in mass of the sample due to oxidation or reduction during measurement. A 0.5 N force was applied to the sample by extension probe, **Figure 2.8b**, at the beginning of the test to achieve the firm contact between the surface of the sample and the expansion probe. The loaded decreased to 0.01 N at the beginning of the test and kept constant during entire testing cycle. The tests

were carried out in Standard mode under the nitrogen that was purged at a rate of 40 ml/min. The SCZ sample was tested using two consecutive heating-cooling thermal cycles. In each cycle, the sample was heated to temperatures from 25 ^{0}C to 900 ^{0}C, with a heating ramp of 5 ^{0}C/min and isothermal holding for 1 hour. After the reaction was complete, the sample was allowed to cool to room temperature. An expansion of the sample during heating and cooling was recorded as a function of temperature.

Figure 2.8 (a) TMA Q400 and (b) probe-glass stage set up

The instantaneous Coefficient of Thermal Expansion (CTE) can be obtained from the slope of the tangent on thermal expansion vs. temperature curve at the particular temperature. The following equation is used to calculate the instantaneous CTE at any temperature:

$$\alpha_L = \frac{1}{L_0}\frac{dL}{dT} \quad \text{.....(2.6)}$$

where L_0 is the original length (thickness of the sample), ΔL is the changes in length (thermal expansion), ΔT is the changes in temperature.

2.2.6 Resonant Ultrasound Spectroscopy (RUS)

Elastic moduli, namely Young's (E) and Shear (G) moduli of SCZ ceramic was determined using Resonance Ultrasound Spectroscope, Quasar International, NM, in the 25-900 ^{0}C temperature range. The sample in the form of disc was placed on three piezoelectric transducers. **Figure 2.9** shows a three-transducer setup that was used in this study for room temperature measurements. For high temperature measurements, **Figure 2.10,** the transducers had similar arrangement to the room temperature set up. The large SiC extension rods were used to transport the waves. The tip of the extension rods is designed to keep transducers unaffected by high temperature in the furnace. The cooling system was used to avoid the damage of transducers at high temperature. One transducer in both setups was used to produce the excitation signal at sweeping frequency in 0.01-300.01 kHz frequency range, and the other two transducers were used to measure resonance response of excited sample.

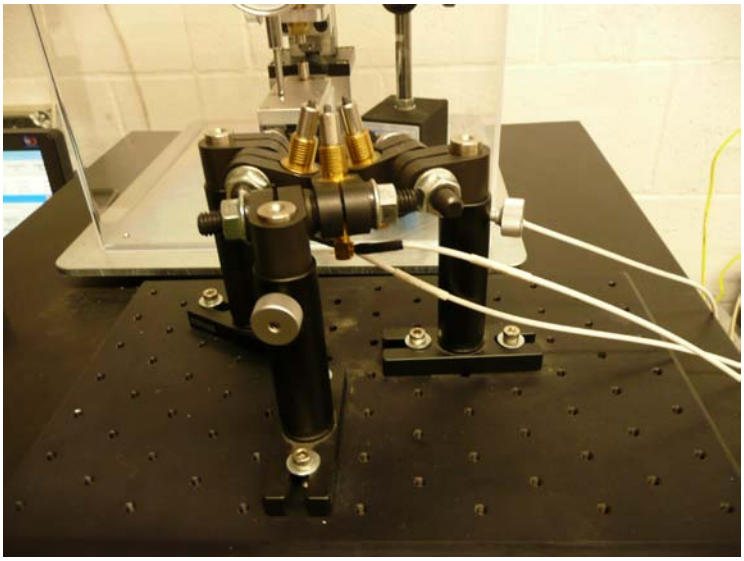

Figure 2.9 RUS setup for measurements at room temperature

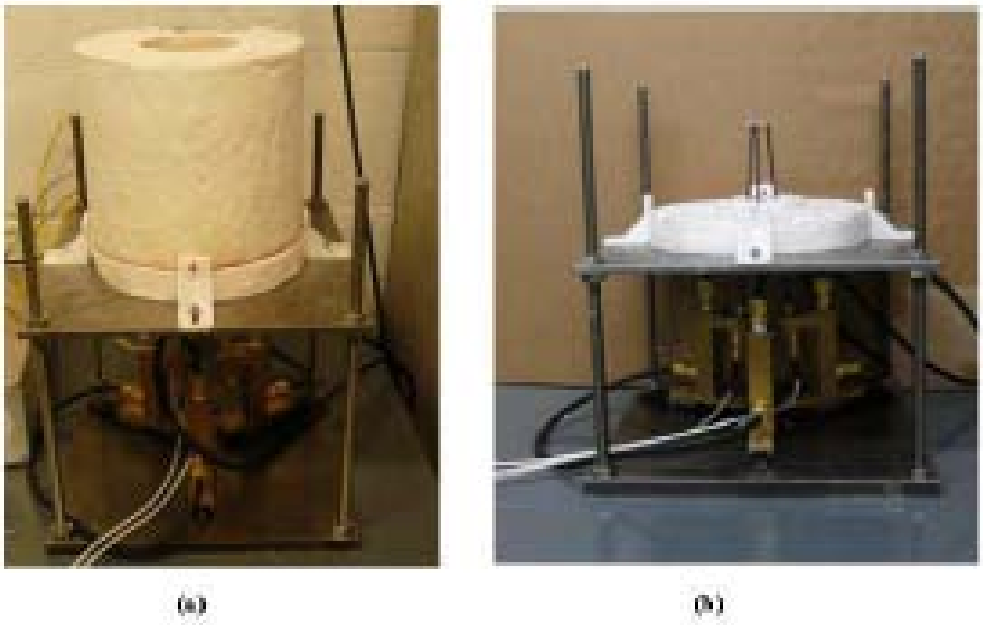

Figure 2.10 (a) RUS setup at high temperature (b) Detailed view of transducers and extension rods. [23]

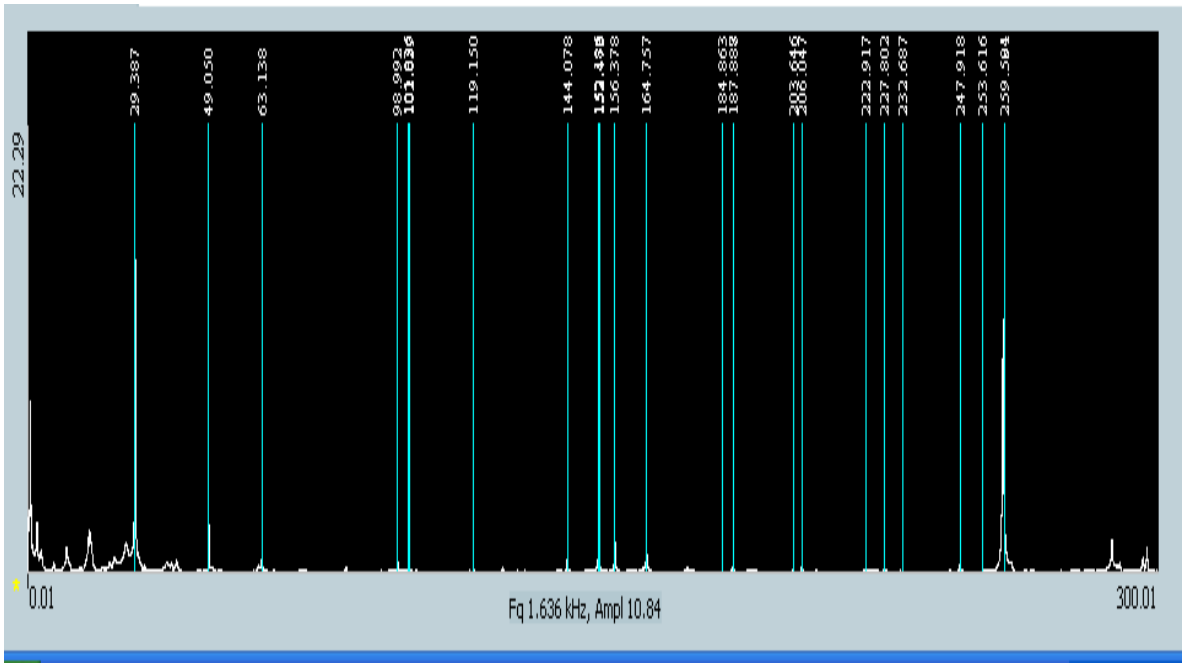

Figure 2.11 Resonant spectrum of SCZ

Figure 2.11 shows the typical resonant spectrum of SCZ samples in 0.01-300.01 kHz frequency range at room temperature. The first 40 resonant peaks were used to determine elastic constants of the isotropic sample, namely c_{11} and c_{44}. The resonant spectra cannot be deconvoluted directly to obtain elastic constants. Instead, multidimensional software RuSpec Quasar International, NM was used to determine elastic constant through iterative process of changing initial values of elastic constant until the root-mean-square (RMS) error between the measured and calculated resonant peaks reaches minimum value. The RMS was calculated using following equation:

$$\chi = \sqrt{\sum_n w_n \frac{(f_{calc} - f_{meas})^2}{f_{meas}^{\ 2}}} \quad \text{.....(2.7)}$$

where w_n is the weight factor given to the normalized difference between the calculated frequencies f_{calc} and measured frequencies f_{meas}. For very few peaks that were missing in the resonant spectra, the weight factor of zero is used in the fitting software.

The following equations were used to calculate Young's modulus (E), shear modulus (G) and poisson's ratio (ν) for known constants c_{11} and c_{44}:

$$c_{44} = \mu = G \quad \text{.....(2.8)}$$

$$E = 2\,\mu\,(1+\nu) \quad \text{.....(2.9)}$$

$$\nu = \frac{c_{12}}{c_{11} + c_{12}} \quad \text{.....(2.10)}$$

where $c_{12}=c_{11}-0.5\,c_{44}$.

2.2.7 Dynamic Mechanical Analysis

The dynamic mechanical behavior of SCZ ceramic was studied using Q800 Dynamic Mechanical Analyzer, TA instruments, DE, USA, in order to determine loss modulus change in the 25-500 ^{0}C temperature range. In order to estimate the absolute position of the draft shaft precisely, the position calibration was determined for the single cantilever clamp. The sample was mounted between the fixed clamp and moving clamp. The moving clamp was connected to the drive motor, where the force was delivered to stress the moving drive block. **Figure 2.12** shows Q800 DMA and the single cantilever clamp.

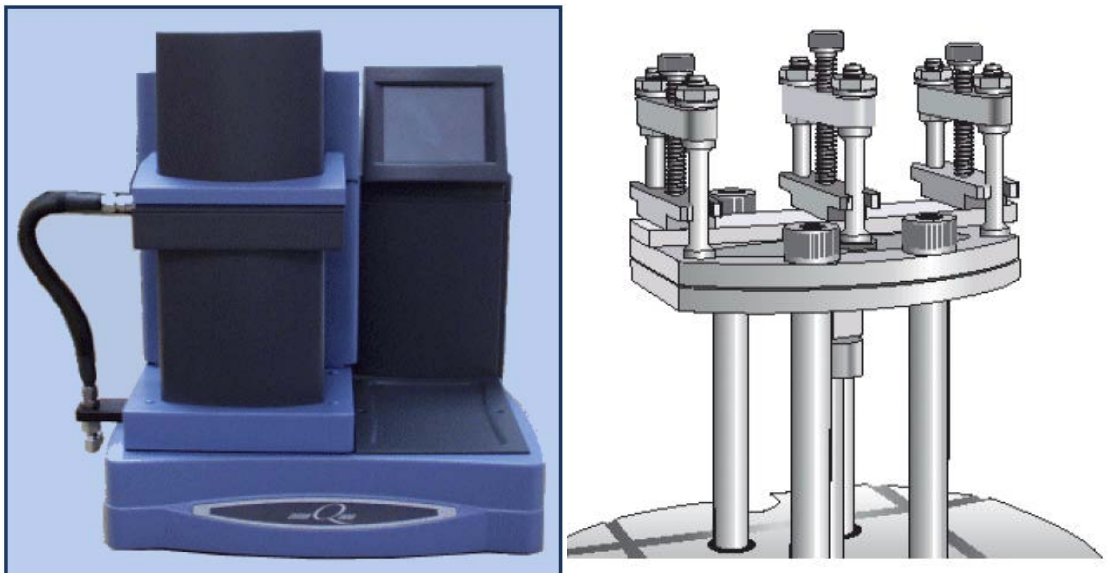

(a) **(b)**

Figure 2.12 (a) Q800 DMA (b) Single/double cantilever clamp

The rectangular SCZ sample with dimensions of 18 mm x 6 mm x 1 mm was tested using DMA under multifrequency strain to evaluate the time, temperature, frequency dependence of loss modulus. Nitrogen at a flow pressure of 50 psi was used as a bearing gas. The SCZ sample was analyzed at equilibration of 25^{0}C, with 10^{0}C

increment per step and isothermal holding for 5 minute. The SCZ sample is analyzed using single cantilever clamp at 0.1 Hz, 1 Hz, 10 Hz and 100 Hz frequency and constant amplitude of ±10 μm relative to the neutral position of the sample. The procedure was repeated until 500 ^{0}C.

2.2.8 Vickers Indentation

The Vickers hardness of SCZ ceramic was obtained using Microhardness Tester LM 300AT, LECO, Michigan, USA, at room temperature. The polished surface sample in the form of disc was placed on stage. Load was applied smoothly to the indenter and hold for 13 second. **Figure 2.13** shows Microhardness Tester LM 300AT that was used in this study.

Figure 2.13 Microhardness Tester LM 300AT

Loads of 50 g, 100 g, 200 g, 500 g, and 1000 g were used for testing. The Vickers indenter creates a square based pyramidal shape indent on the surface of the sample. The indentation diagonals of the indents were measured for each load and these length measurements were used to calculate the Vickers hardness number (HV). The following equation is used to calculate the Vickers hardness number at any load:

$$HV = 1.854 \left(\frac{P}{d^2} \right) \quad \text{.....(2.11)}$$

where P is the applied load in N, and d is the average length of the two diagonals of the indentation, mm. Five indentations were made on the polished surface sample for each load. **Figure 2.14** shows typical indentations for each load as seen using Digital Microscope VHX-600.

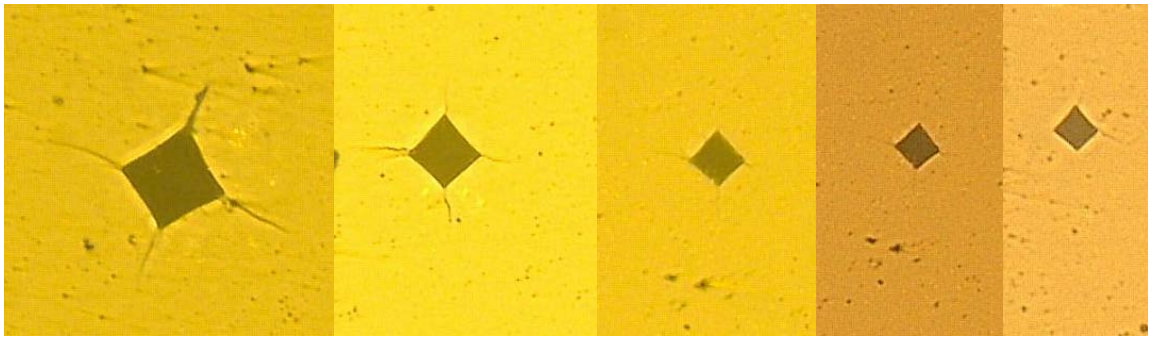

(a) **(b)** **(c)** **(d)** **(e)**

Figure 2.14 Vickers indents made in SCZ ceramic using (a) 1000 g (b) 500 g (c) 200 g (d) 100 g and (e) 50 g test forces

The length of the corner cracks (d_c) and the length of the two diagonals of indentation (d) were measured using Digital Microscope VHX-600. The Vickers hardness was then calculated analytically using Eq. 2.11 from average length of diagonals, while the length of the corner cracks were used to estimate fracture toughness of the examined samples.

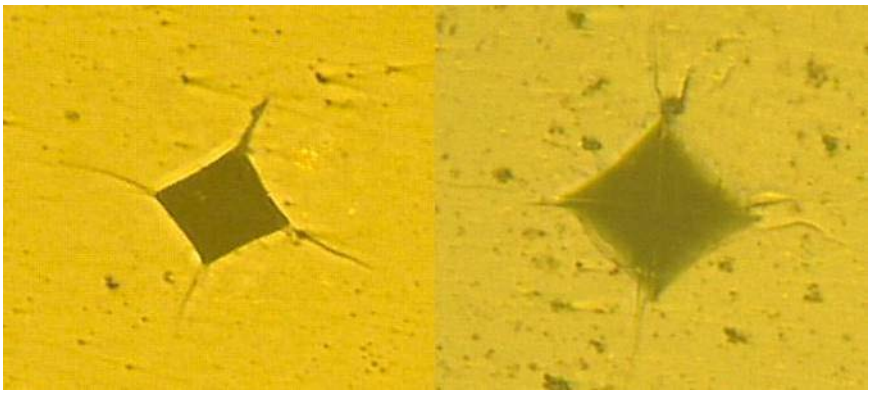

(a) **(b)**

Figure 2.15 Surface appearance of crack system (a) before polishing and (b) after polishing for four minute at 1000 g

The Vickers indents were re-polished for four minutes to determine the character of the corner cracks at the indent. **Figure 2.15** shows the surface appearance of crack system before and after polishing for four minutes at 1000 g. After the surface material have been repolished, the morphology of the corner cracks suggests that median corner cracks developed during indentation. In the past, several researchers had attempted to determine the fracture toughness (K_{IC}) for median crack at room temperature using Vickers indents. The most common methods are summarized as follows:

- "Evaluation of K_{ic} of brittle solids by the indentation method with low crack to indent ratios" – This method was pioneered by K. Niihara, R. Morena, D. P. H. Hasselman [118]. Here the formation of median crack is equivalent to a penny-shaped crack, and it split with a force at its center. The fracture toughness (K_{ic}) for median crack is given by:

$$Kic = \left(\frac{0.129H\sqrt{a}}{\phi}\right)\left(\frac{E\phi}{H}\right)^{0.4}\left(\frac{c}{a}\right)^{-1.5} \quad \text{.....(2.12)}$$

where H is the hardness, E is Young's modulus, a is the half diagonal of the Vickers indents, c is the radius of the surface crack and ϕ is the constraint factor (~3).

- "Indentation microfracture in the Palmqvist crack regime: implication for fracture toughness evaluation by the indentation method" – This method was pioneered by James Lankford [119]. According to this model, the fracture toughness (K_{ic}) for median crack can be estimated as:

$$Kic = \left(\frac{0.142H\sqrt{a}}{\Phi}\right)\left(\frac{E\Phi}{H}\right)^{0.4}\left(\frac{c}{a}\right)^{-1.56} \quad \text{.....(2.13)}$$

  where H is the hardness, E is Young's modulus, a is the half diagonal of the Vickers indents, c is the radius of the surface crack and Φ is the constraint factor (~3).

- "Elastic/plastic indentation damage in ceramics: the median/radial crack system" – This method was pioneered by B. R. Lawn, A. G. Evans and D. B. Marshall [120]. This method involves a point load in an elastic-plastic semi infinite solid. The following formula is used to calculate the fracture toughness (K_{ic}) for median crack according to this model:

$$Kic = 0.028H\sqrt{a}\left(\frac{E}{H}\right)^{1/2}\left(\frac{c}{a}\right)^{-3/2} \quad \text{.....(2.14)}$$

  where H is the hardness, E is Young's modulus, a is the half diagonal of the Vickers indents, c is the radius of the surface crack.

- "A critical evaluation of indentation techniques for measuring fracture toughness: I, direct crack measurements". This method was pioneered by G. R. Anstis, P. Chantikul, B. R. Lawn and D. B. Marshall [121]. This process involves a measurement of radial cracks as a function of indentation load. Here the radial crack corresponds to the remaining component of the contact field. The fracture toughness (K_{ic}) for median crack can be written as follows:

$$Kic = 0.016\left(\frac{E}{H}\right)^{1/2}\left(\frac{P}{c^{3/2}}\right) \quad \text{.....(2.15)}$$

  where H is the hardness, E is Young's modulus, P is peak load, c is the radial/median crack.

All four methods, Eqs. 2.12-2.15 were used in present study to estimate indentation fracture toughness of SCZ samples.

2.2.9 Four Point Bending Test

The flexural strength of SCZ was measured by four point bending test. The tests were performed using MTS 810 Material Test System at room temperature, 400 ^{0}C, 600 ^{0}C and 800 ^{0}C in air. The samples were machined by BOMAS Inc. Somerville, MA following the ASTM Standard C 1161 recommendations for four point bending testing of ceramics. **Figure 2.16** shows the four point bending sample configuration. A sample is loaded at two locations 20 mm from each other and 10 mm from supporting points as it is illustrated in **Figure 2.16**.

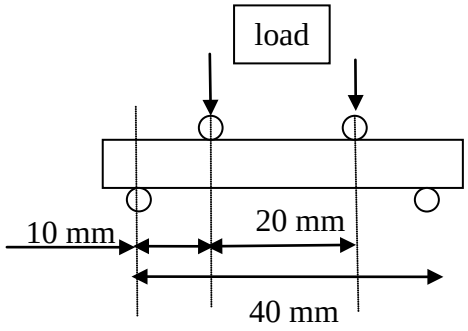

Figure 2.16 Four point bending sample configuration

The test fixture for the four point bending is designed to ensure that supporting and loading pivots and sample stay in desired configuration during testing. For room temperature testing, the test fixture is made from stainless steel. **Figure 2.17** shows the test fixture setup for room temperature testing. The distance between centers of loading pins (rollers) was 20 mm and the distance between supporting ones was 40 mm. All four bearings can roll freely to minimize effect of friction forces. The two supporting and loading pivots were kept parallel to each other. The stainless steel semisphere with 1/8 inch diameter was placed on the top part of the test fixture.

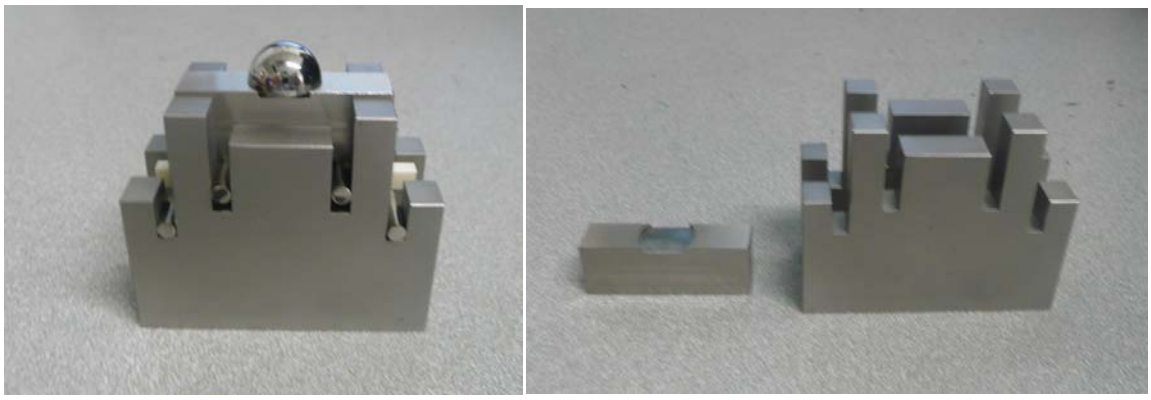

Figure 2.17 (a) Test fixture setup at room temperature (b) Detailed view of top part and bottom part of test fixture

Figure 2.18 shows the test fixture setup at high temperature. For high temperature testing, the test fixture is made from SIC carbide. The distance between centers of loading pins (rollers) was also 20 mm and the distance between supporting ones was 40 mm. All four ceramic pins can roll freely. The alumina semisphere with 3/8 inch diameter is placed on the top part of the test fixture.

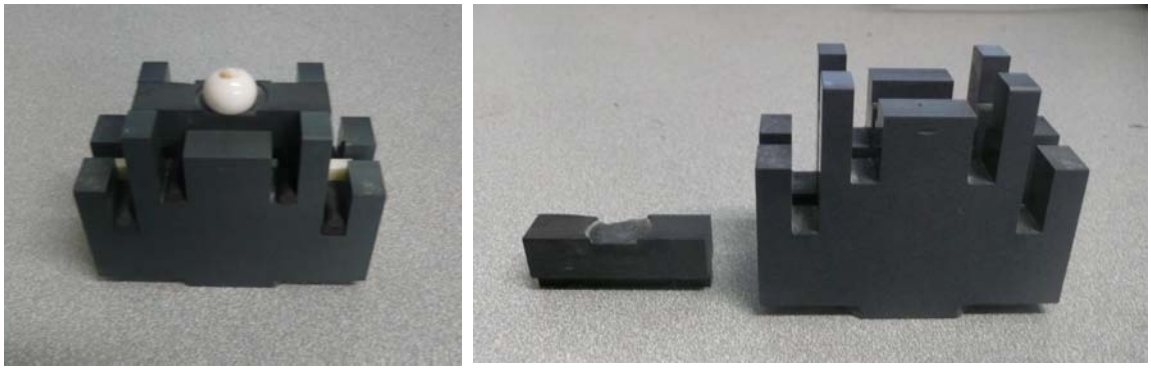

Figure 2.18 (a) Test fixture setup at high temperature (b) Detailed view of top part and bottom part of test fixture

The thickness, weight and length of the sample were measured before the test. After sample was placed in the testing fixture, the distance between loading and supporting pins was measured. SCZ sample was tested using ramp segment with the crosshead displacement rate of 0.25 in/min at MTS universal servo-hydraulic testing

machine. Level crossing acquisition method was chosen for axial displacement signal with 0.001 mm increment. Axial force, displacement and maximum load point were recorded during testing. The following formula was used to calculate the flexural strength of a beam in four point bending test:

$$\sigma = \left(\frac{3}{4}\right)\frac{PL}{bd^2} \quad \text{.....(2.15)}$$

where P is break force, L is outer (supporting) span, B is sample width, and d is sample thickness. At least 10 specimens were tested at each temperature and average flexural strength was calculated.

Figure 2.19 shows MTS 810 Material Test System universal servo-hydraulic machine that was used in the present study.

Figure 2.19 MTS 810 Material Test System setup for compression test at (a) room temperature and (b) high temperature

Probability of survival (P_s) for four point bending loading was determined using Weibul analysis at each temperature. The sample was ranked in category of increasing strength, 1, 2, 3,…,j , j+1,…N, where N is the total number of samples. The probability of survival for the first sample was 1-1 / (N+1); for the second sample was 1-2 / (N+1); for the jth sample was 1-j / (N+1), etc. The following analysis is used in Weibull statistics:

$$\ln\left[\ln\left(\frac{1}{P_S}\right)\right] = m\ln\left(\frac{\sigma}{\sigma_0}\right)^m = m\ln\sigma - m\ln\sigma_0 \quad \text{.....(2.16)}$$

The data were plotted at $-\ln\ln(1/P_s)$ vs. $\ln\ \sigma$ and fitted by straight line to determine parameters of Weibull distribution, namely m (Weibull modulus) and σ_0.

3. RESULTS

3.1 Microstructure

3.1.1 Grain Size

Figure 3.1 shows the optical microscopy of the thermally etched SCZ sample with grain lengths along three lines that were used to determine average grain size using intercept method. In general, grains have polygonal shape. This microphotograph also show a few pores or pull outs formed during specimen preparation. Neither continuous porosity, nor impurities or secondary phases were observed in the examined sample.

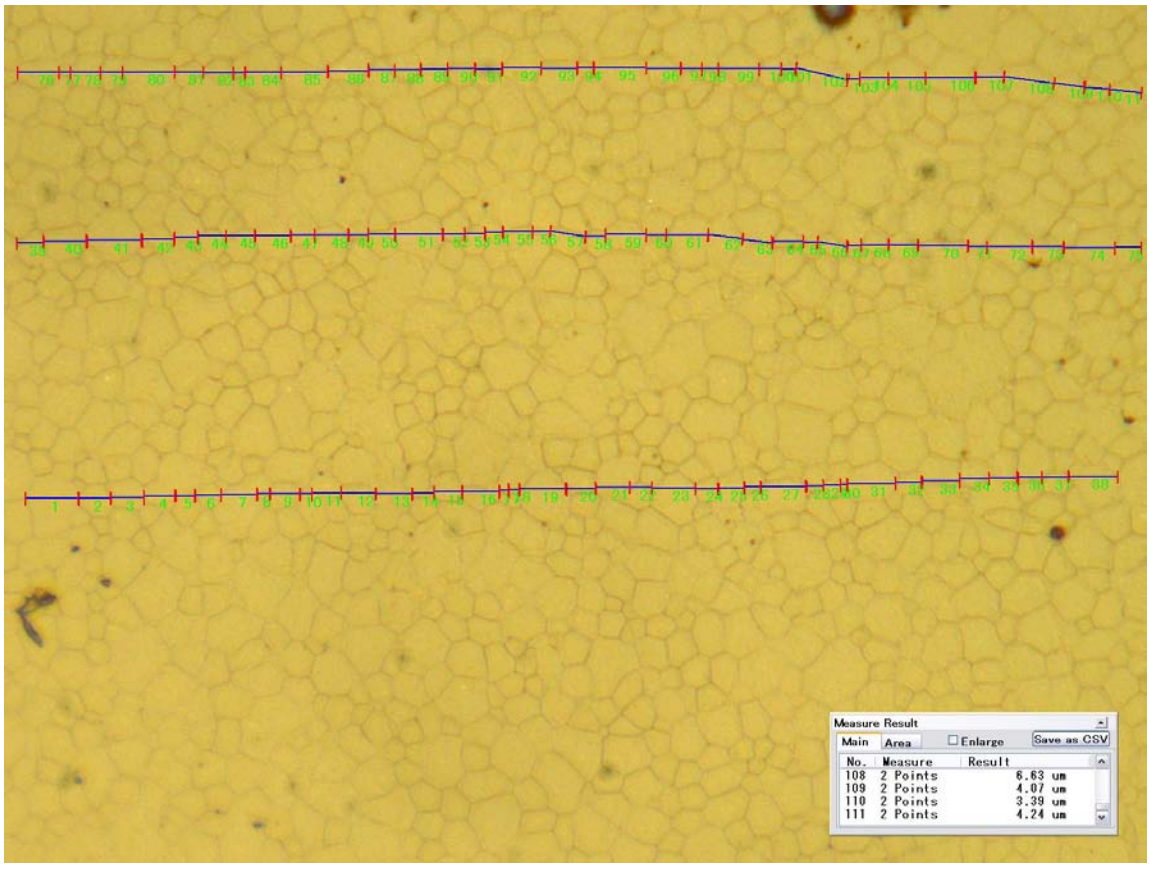

Figure 3.1 Microstructure of SCZ bar

The average and standard deviation of grain size in the sample sintered at 1500 ^{0}C for 2 hours are given in Table 3.1. An amount of 111 grains are measured. The grain size distribution is fairly homogeneous, and the average grain size is 4.008 μm.

Table 3.1 Grain size of SCZ bar

Sample	Grain Size (μm)	
	Average	Std. Dev.
SCZ bar	4.008	1.496

3.1.2. Chemical Composition

Figures 3.2 and **3.3** shows a BSE SEM image of polished SCZ sample. The BSE images show relatively homogeneous chemical composition of the sample with small amount of inclusions and some areas with compositional inhomogeneity. Seven points were selected to analyze the chemical composition of SCZ by EDS and WDS.

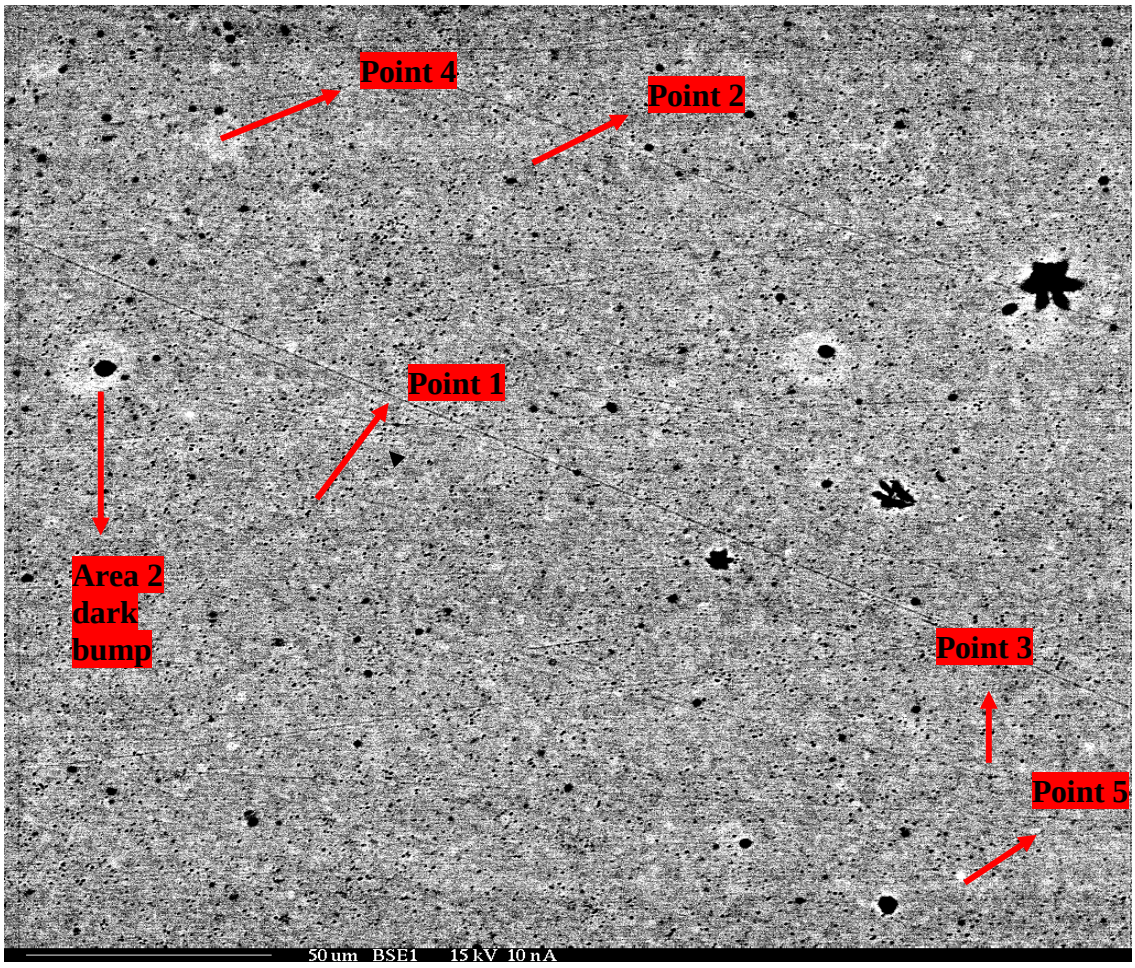

Figure 3.2 BSE images of a polished SCZ sample (scale bar = 50 μm)

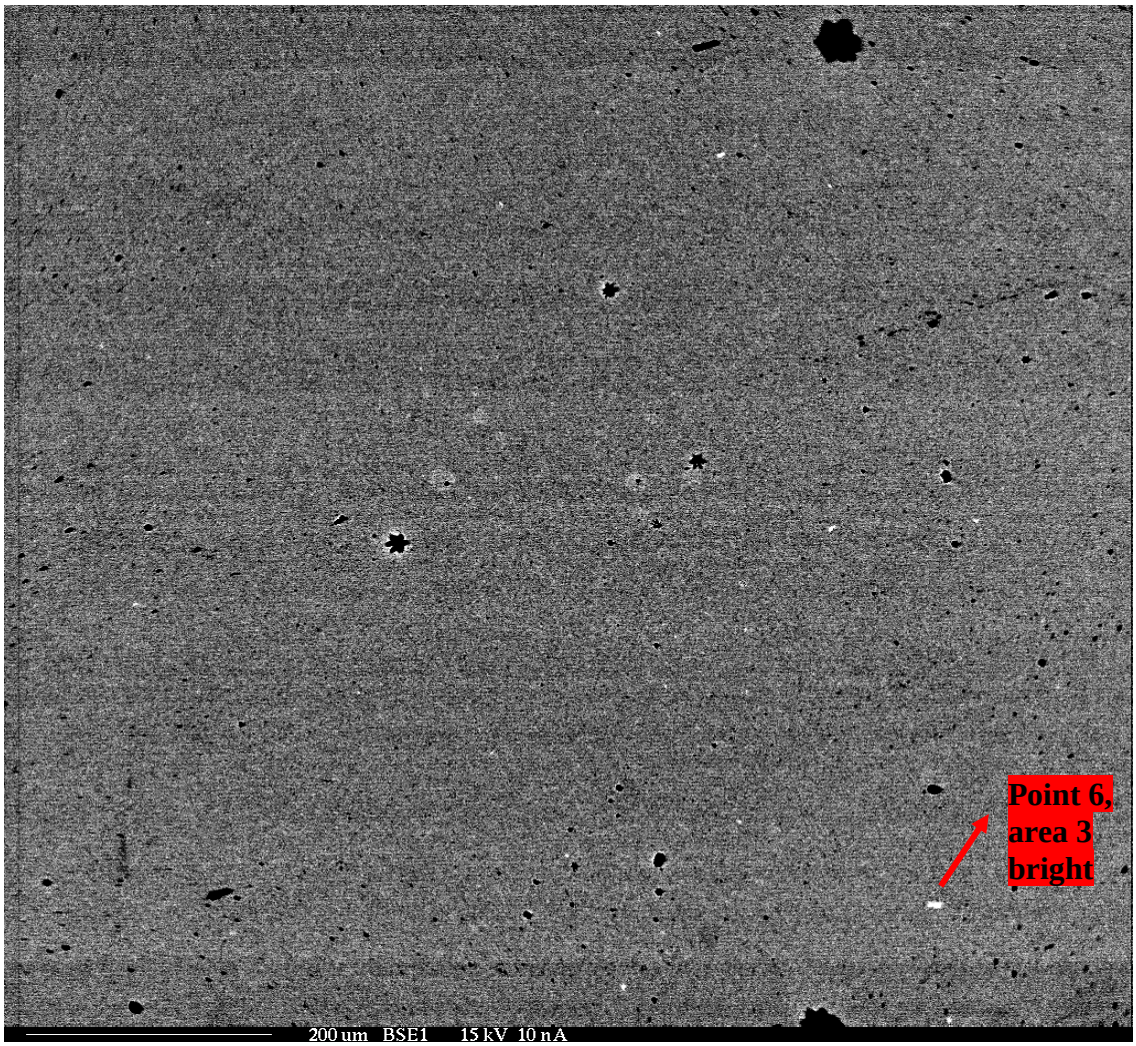

Figure 3.3 BSE images of a polished SCZ sample (scale bar = 200 μm)

Figures 3.4 - 3.6 shows EDS spectra for selected points, namely Point 1, 2 and 3 that are shown in **Figure 3.2**. This result indicates that brighter areas in **Figure 3.2** contains smaller amount of Sc and Ce, while darker gray areas are rich in Sc and Ce. The dark area (Area 2 in **Figure 3.2**) contains carbon, most likely an artifact from specimen preparation.

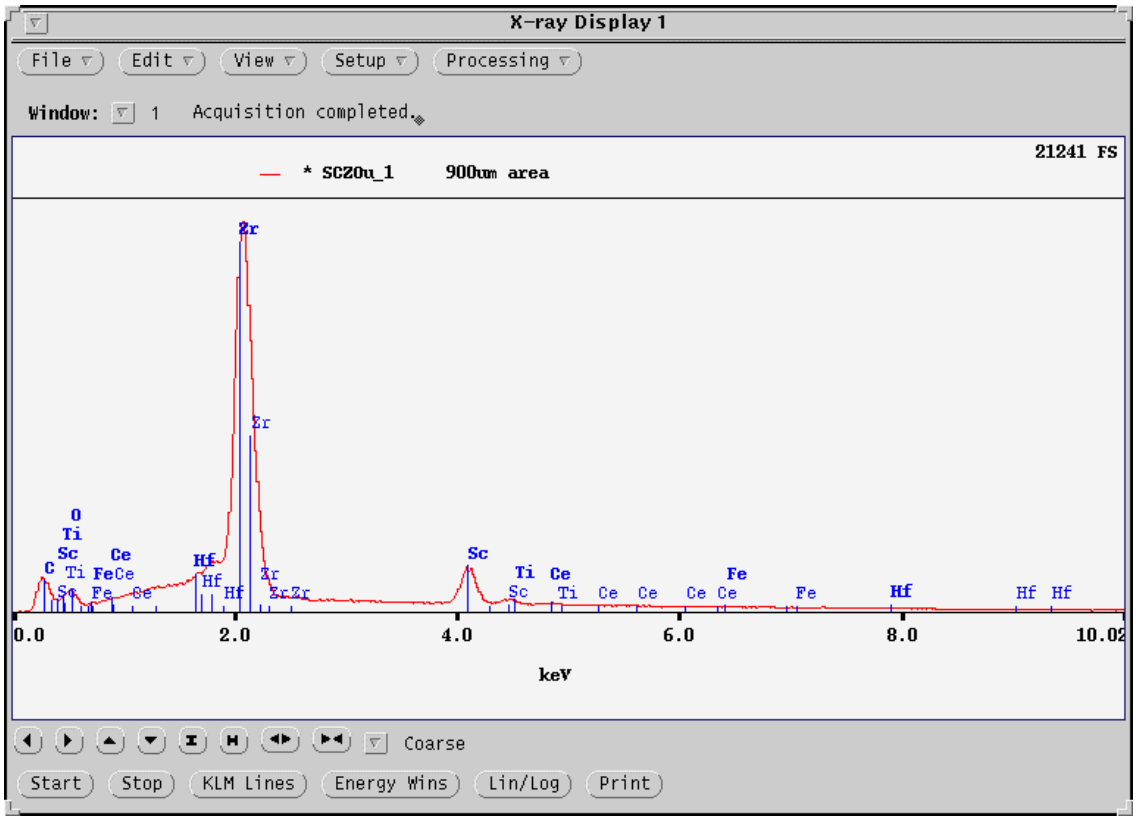

Figure 3.4 EDS spectrum of a polished SCZ sample (scale bar = 900 µm)

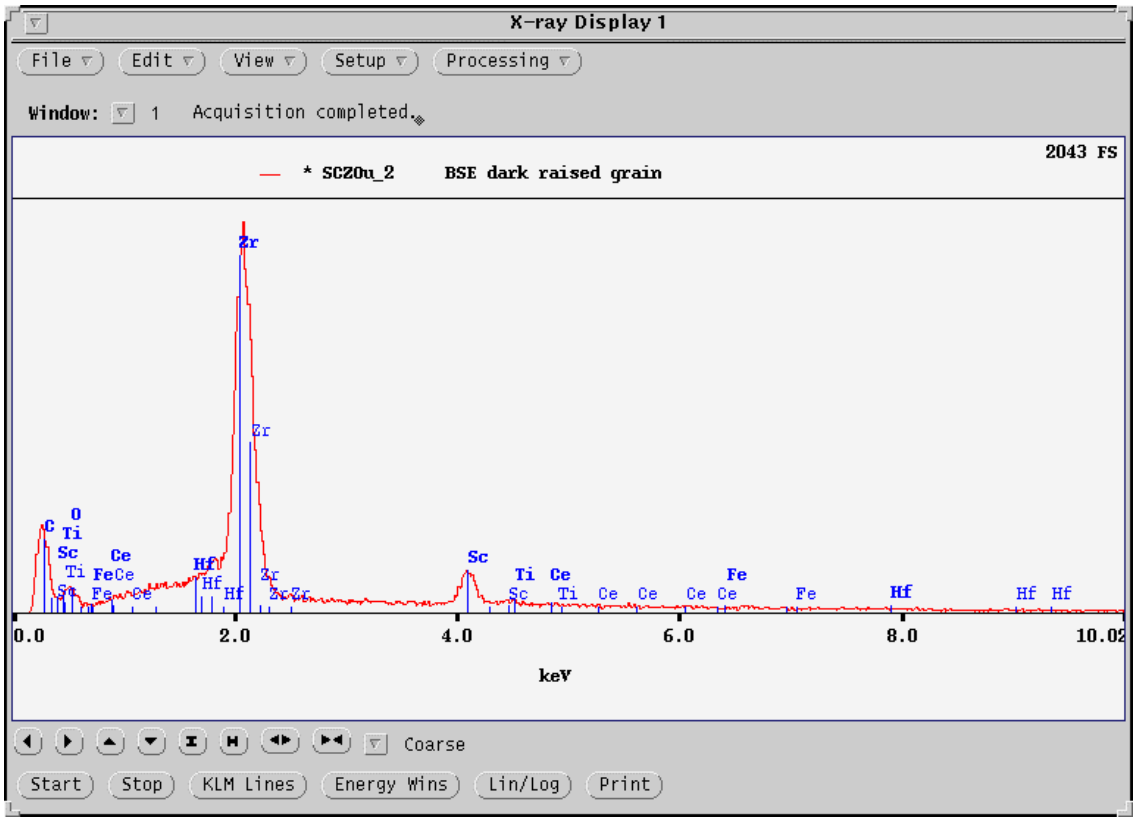

Figure 3.5 EDS spectrum of a polished SCZ sample at dark area, point 2 in Figure 3.2

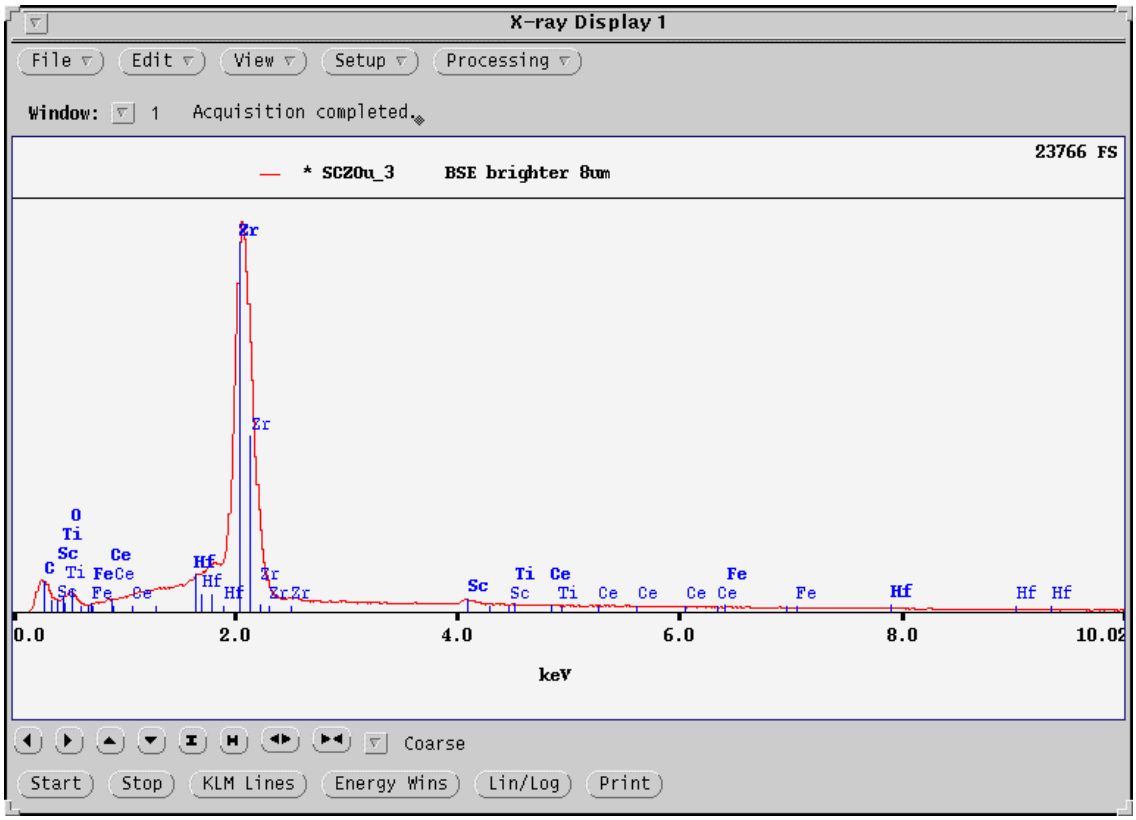

Figure 3.6 EDS spectrum of a polished SCZ sample at brighter area, point 3 in Figure 3.2

The quantitative composition was determined in six different points labeled in **Figures 3.2** and **3.3** by WDS. Table 3.2 shows weight percent, wt% and atomic percent, at% of Zr, Sc, Ce, Hf, Ti, and O in different locations.

Table 3.2 Quantitative composition of SCZ sample

	Zr	Sc	Ce	Hf	Ti	O
Point 1 in **Figure 3.2**						
wt %	63.131	7.073	1.148	1.498	0.003	26.389
at %	27.513	6.255	0.326	0.334	0.002	65.570

Table 3.2 Continued

Point 2 in **Figure 3.2**

wt %	62.469	7.332	1.116	1.570	0.012	26.309
at %	27.292	6.500	0.318	0.350	0.010	65.530

Point 3 in **Figure 3.2**

wt %	63.089	7.259	1.176	1.476	0.005	26.476
at %	27.394	6.396	0.333	0.328	0.004	65.545

Point 4 in **Figure 3.2**

wt %	62.127	7.180	1.189	1.288	0.001	26.063
at %	27.402	6.426	0.342	0.290	0.001	65.539

Point 5 in **Figure 3.2**

wt %	66.386	3.424	0.715	1.620	0.000	25.529
at %	30.151	3.156	0.211	0.376	0.000	66.105

Point 6 in **Figure 3.2**

wt %	70.081	1.252	0.440	1.746	0.010	25.648
at %	31.848	1.155	0.130	0.406	0.009	66.453

3.1.3. X-Ray Diffraction (XRD)

The XRD pattern of SCZ at room temperature is shown in **Figure 3.7**. A pure cubic phase of SCZ sample was identified by X-ray diffraction (XRD) at room temperature.

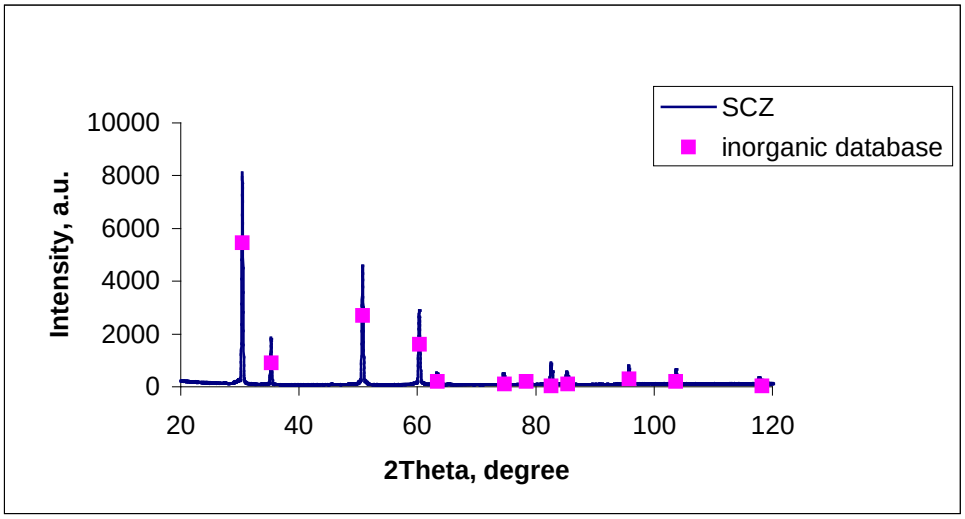

Figure 3.7 XRD pattern of SCZ at room temperature. Pink dots shows position for cubic zirconia from Inorganic Crystal Database [122]

3.2. Density and Porosity Measurement

Table 3.3 shows the density and porosity measured for seven different SCZ samples, namely two pellets and five bars. Total porosity is found to be below 2%. However, two pellets have been found to have highest closed porosity and lowest open porosity.

Table 3.3 Densities and porosities of examined SCZ materials

Sample	Theoretical density (g/cm3)	Archimedian density (g/cm^3)	Open porosity	Closed Porosity
E2-N-01 pellet	5.74	5.623	0.066	1.974
E2-N-06 pellet	5.74	5.611	0.091	2.146
E2-N-01 bar	5.74	5.716	0.154	0.265
E2-N-02 bar	5.74	5.696	0.329	0.426
E2-N-03 bar	5.74	5.720	0.044	0.303
E2-N-04 bar	5.74	5.699	0.440	0.276
E2-N-05 bar	5.74	5.731	0.044	0.108

3.3. Coefficient of Thermal Expansion

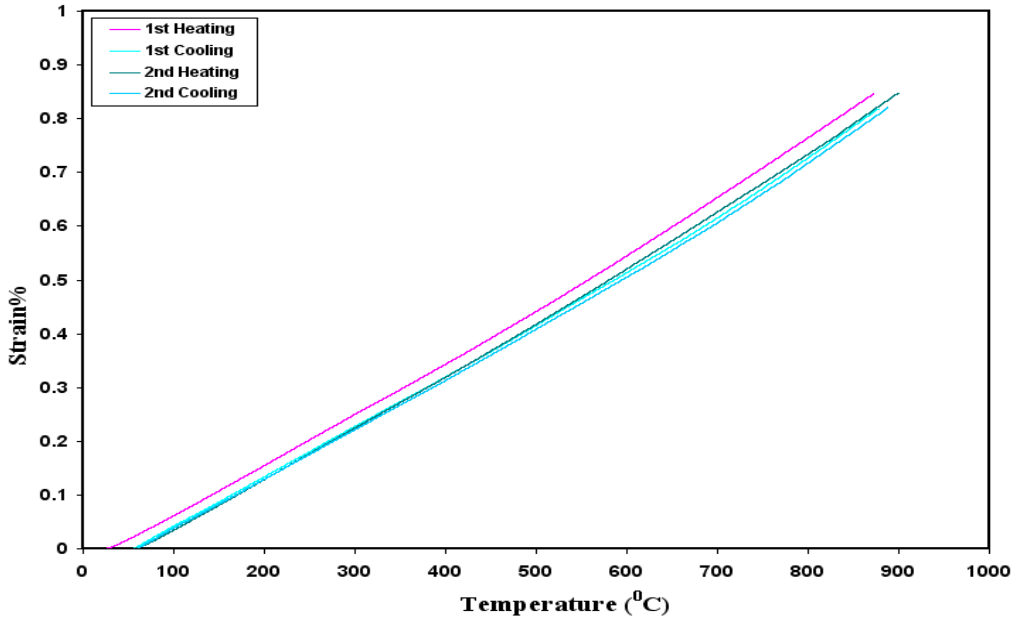

Figure 3.8 Thermal expansion of SCZ material

Figure 3.8 shows thermal expansion of SCZ measured in two heating-cooling cycles in 25-900 ^{0}C temperature range, while **Figure 3.9** shows instantaneous CTE determined using Eq. 2.5. The instantaneous CTE is almost constant in 25-400 ^{0}C temperature range. Above that 400 ^{0}C, it gradually increases with temperature from 8.726×10^{-6} at 400 ^{0}C to 1.16×10^{-5} at 890 ^{0}C.

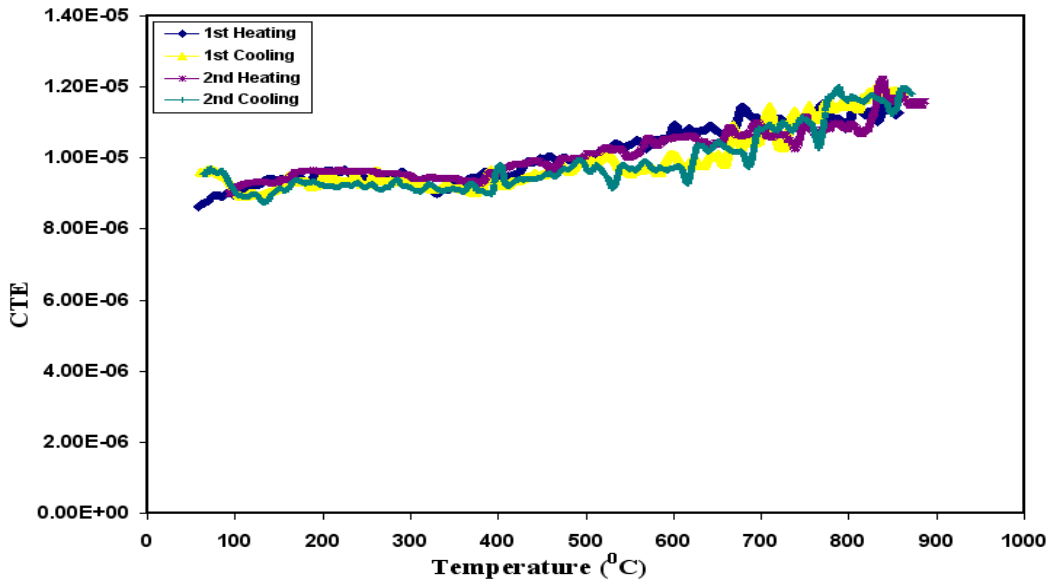

Figure 3.9 Instantaneous coefficient thermal expansion vs. Temperature of SCZ material

Figure 3.9 shows that the slope of the instantaneous coefficient thermal expansion curves increases with temperature at temperatures above approximately 400 ^{0}C, implying a loss of oxygen at higher temperatures [123, 124]. The weight change of SCZ sample was fully reversible over heating and cooling in air.

3.4. Room and High Temperature Elastic Moduli

Figure 3.10 shows change in elastic moduli, namely Young's modulus, E, and shear modulus, G, with temperature for SCZ samples determined by Resonant Ultrasound spectroscopy. The elastic moduli decrease slightly in 25-350 ^{0}C temperature range, followed with significant drop in the magnitude of elastic moduli in 400-600 ^{0}C temperature range. Above 600 ^{0}C, elastic moduli increase slightly with temperature up to 900 ^{0}C.

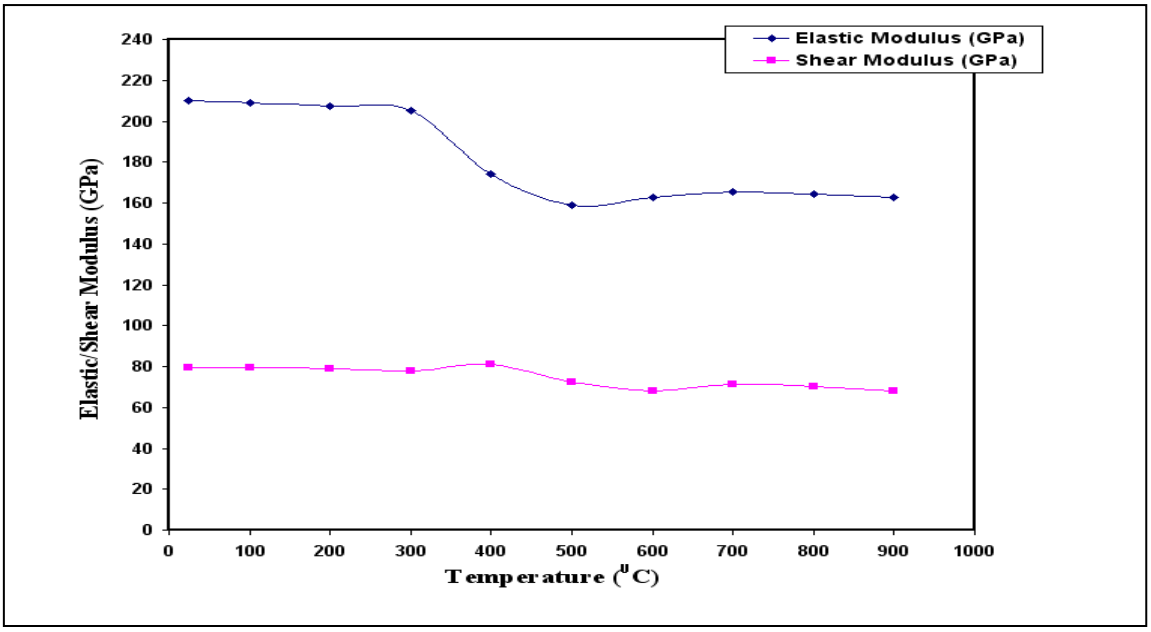

Figure 3.10 Elastic and shear moduli of SCZ for different temperature

3.5. Dynamic Mechanical Analysis

Figure 3.11 shows the change of loss modulus with temperature measured by DMA for SCZ sample. Loss modulus spectrum shows frequency dependent peak in 300-400 ^{0}C temperature range. The position of the peak shifts toward higher temperatures with increasing frequency. In addition, the smaller frequency dependent relaxation peak can be observed at around 100 ^{0}C.

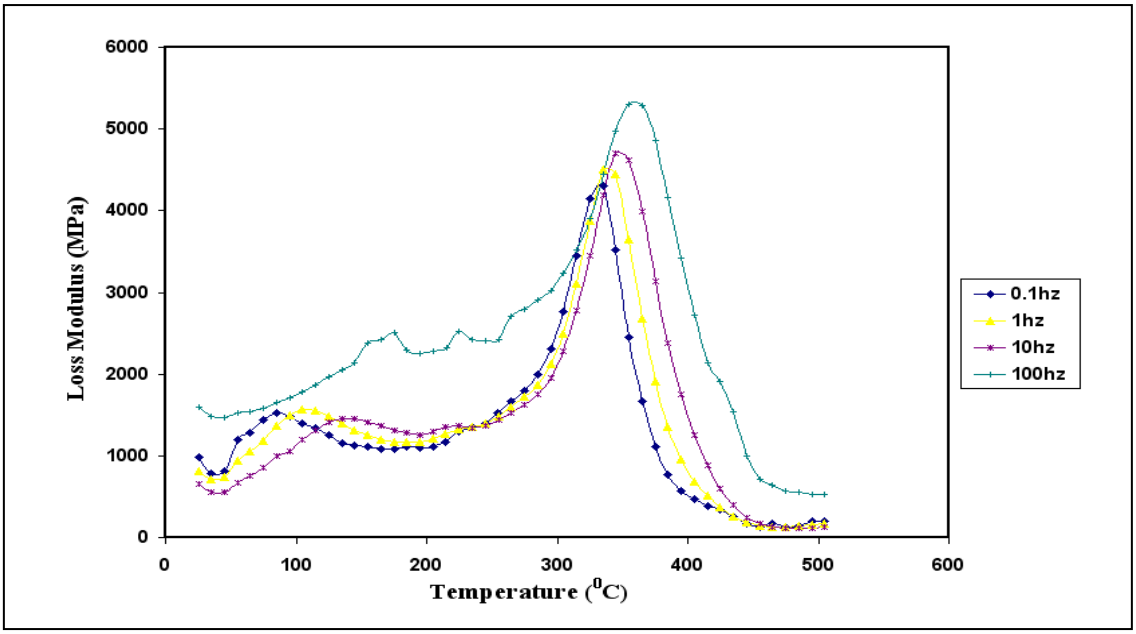

Figure 3.11 Loss modulus of SCZ at different frequencies as a function of temperature

3.6. Hardness

The plot of average Vickers hardness number (HV) vs. applied load is shown in **Figure 3.12**. The plot shows a typical decreasing relationship between the average hardness and force.

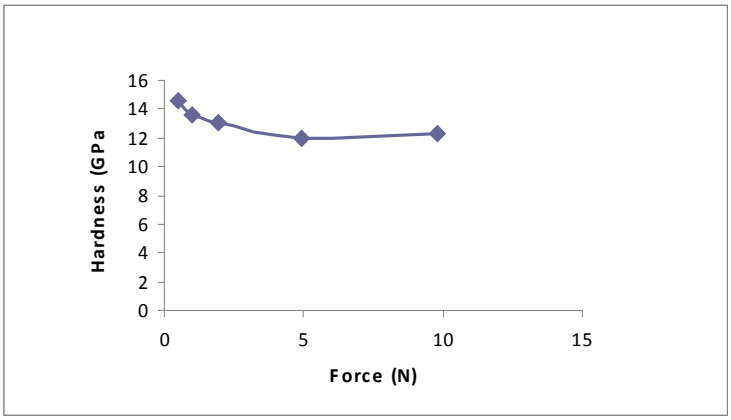

Figure 3.12 Hardness vs force of SCZ

3.7. Indentation Fracture Toughness

The average values and standard deviations of indentation fracture toughness were shown in **Table 3.4** for examined SCZ samples. Four different methods that were described in more details in previous sections were used to determine fracture toughness from the length of the median corner cracks, **Figure 2.14 and 2.15**. The fracture toughness depends on the measurement method that was employed to calculate indentation fracture toughness. The higher average fracture toughness values, namely 4.062, and 4.298 MPa-$m^{1/2}$ were obtained using Niihara's et al. [118] and Lankford's [119] method, respectively.

Table 3.4 Fracture toughness of SCZ materials from Vickers indents

Method	Equation for Kic (median cracks) from vickers indents	Fracture toughness for median cracks (Mpa-m1/2)	
		Avg.	Std. Dev.
Niihara et al.	$Kic = \left(\frac{0.129H\sqrt{a}}{\phi}\right)\left(\frac{E\phi}{H}\right)^{0.4}\left(\frac{c}{a}\right)^{-1.5}$	4.062	0.529
Lankford	$Kic = \left(\frac{0.142H\sqrt{a}}{\Phi}\right)\left(\frac{E\Phi}{H}\right)^{0.4}\left(\frac{c}{a}\right)^{-1.56}$	4.298	0.584
Lawn et al.	$Kic = 0.028H\sqrt{a}\left(\frac{E}{H}\right)^{1/2}\left(\frac{c}{a}\right)^{-3/2}$	2.252	0.295
Anstis et al.	$Kic = 0.016\left(\frac{E}{H}\right)^{1/2}\left(\frac{P}{c^{3/2}}\right)$	2.776	0.363

3.8. Point Bending Strength

The results of 4-point bending are shown in **Tables 3.5-3.8** while **Figure 3.13** shows the average values and standard deviations of flexural strength of SCZ determined in 4-point bending in the 25 ^{0}C-800 ^{0}C temperature range. The bending strength of SCZ depends on the testing temperature. The average strength increases from 126.42 MPa at

room temperature to 173.74 MPa at 400 ^{0}C. The SCZ has a minimum average strength of 94.47 MPa at 600 ^{0}C. Above 400 ^{0}C, average flexural strength increases again to 146.36 MPa.

Table 3.5 Results of 4-point bending tests at room temperature. d, b, l, P, and σ are defined in Eq. 2.15, while P_s is defined in Eq. 2.16

Sample number	d	b	l	P	σ	lnσ	P_s	ln(ln(1/P_s))
	mm	mm	mm	lbs	MPa			
1	3.992	2.98	39.41	26.56	73.82	4.30	0.92	2.44
2	3.986	2.95	39.42	27.81	77.39	4.35	0.80	1.49
3	3.978	2.98	39.40	28.47	79.30	4.37	0.68	0.95
4	3.996	2.98	39.43	29.25	81.08	4.40	0.56	0.54
5	3.992	2.97	39.40	30.12	83.77	4.43	0.44	0.20
6	3.988	2.98	39.43	43.27	120.67	4.79	0.32	-0.13
7	3.984	2.98	39.42	80.56	224.75	5.41	0.20	-0.47
8	3.994	2.96	39.37	97.52	270.55	5.60	0.08	-0.91
Average					126.42			
Standard deviation					77.22			

Table 3.6 Results of 4-point bending tests at 400 ^{o}C. d, b, l, P, and σ are defined in Eq. 2.15, while P_s is defined in Eq. 2.16

Sample number	d	b	l	P	σ	lnσ	P_s	ln(ln(1/P_s))
	mm	mm	mm	lbs	MPa			
1	3.98	2.98	41.28	38.63	112.48	4.72	0.92	2.44
2	3.99	2.99	41.21	47.37	136.67	4.92	0.80	1.49
3	3.99	2.98	41.32	50.42	146.74	4.99	0.68	0.95

Table 3.6 Continued

4	3.98	2.98	41.16	58.04	168.79	5.13	0.56	0.54
5	3.99	2.98	41.22	58.24	169.15	5.13	0.44	0.20
6	3.99	2.98	41.25	59.87	173.89	5.16	0.32	-0.13
7	3.99	2.98	41.20	72.98	211.51	5.35	0.20	-0.47
8	3.98	2.97	41.33	92.67	270.69	5.60	0.08	-0.91
Average					173.74			
Standard deviation					48.88			

Table 3.7 Results of 4-point bending tests at 600 ^{o}C. d, b, l, P, and σ are defined in Eq. 2.15, while P_s is defined in Eq. 2.16

Sample number	d	b	l	P	σ	lnσ	P_s	ln(ln(1/P_s))
	mm	mm	mm	lbs	MPa			
1	3.98	2.97	41.29	20.40	59.68	4.09	0.92	2.44
2	3.99	2.98	41.34	20.68	60.18	4.10	0.80	1.49
3	3.99	2.98	41.23	23.75	68.95	4.23	0.68	0.95
4	3.98	2.96	41.39	24.46	71.83	4.27	0.56	0.54
5	3.99	2.99	41.23	25.11	72.69	4.29	0.44	0.20
6	3.99	2.98	41.23	28.40	82.50	4.41	0.32	-0.13
7	3.99	2.98	41.36	28.39	82.63	4.41	0.20	-0.47
8	3.99	2.98	41.32	32.40	94.47	4.55	0.08	-0.91
Average					74.12			
Standard deviation					11.92			

Table 3.8 Results of 4-point bending tests at 800 ^{o}C. d, b, l, P, and σ are defined in Eq. 2.15, while P_s is defined in Eq. 2.16

Sample number	d	b	l	P	σ	lnσ	P_s	ln(ln(1/P_s))
	mm	mm	mm	lbs	MPa			
1	3.99	2.98	41.28	19.96	57.99	4.06	0.92	2.44
2	3.98	2.98	41.31	33.88	98.74	4.59	0.80	1.49
3	3.98	2.97	41.21	38.40	112.19	4.72	0.68	0.95
4	4.00	2.98	41.22	41.74	120.46	4.79	0.56	0.54
5	3.98	2.98	41.15	43.12	125.19	4.83	0.44	0.20
6	3.98	2.98	41.32	45.74	133.76	4.90	0.32	-0.13
7	3.98	2.98	41.16	69.36	201.83	5.31	0.20	-0.47
8	3.99	2.98	41.20	110.80	320.70	5.77	0.08	-0.91
Average					146.36			
Standard deviation					81.06			

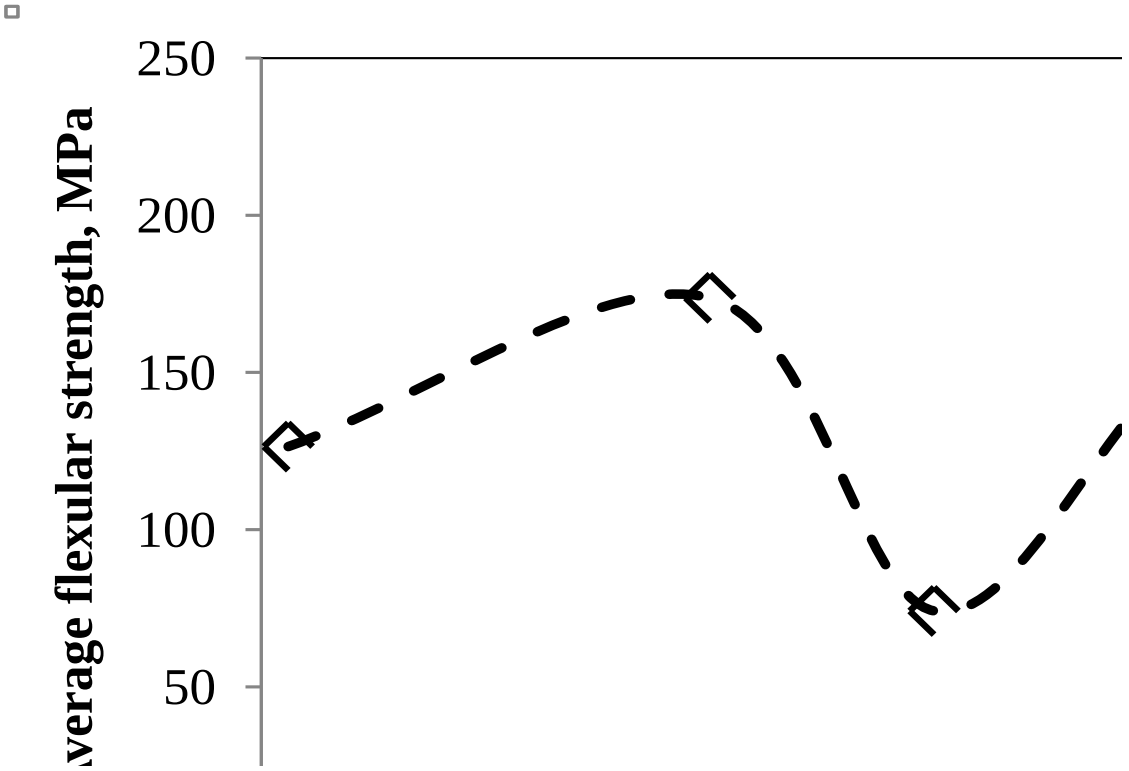

Figure 3.13 Average flexural strength vs. Temperature of SCZ. Error bars indicate standard deviation

The probability of failure for each sample was calculated using procedure described in previous section and the values are shown in Tables 3.5-3.8. Those values were used to plot Weibull plots for SCZ samples at different temperatures, **Figure 3.14**. Results shown in **Figure 3.14** that shows that Weibull plots can be fitted by two straight lines in two different regions-low and high stress region-for all temperatures except 600 ^{0}C. Results of Weibull analysis, namely Weibull modulus, m, and Weibull strength, σ_0 are shown in **Table 3.9**.

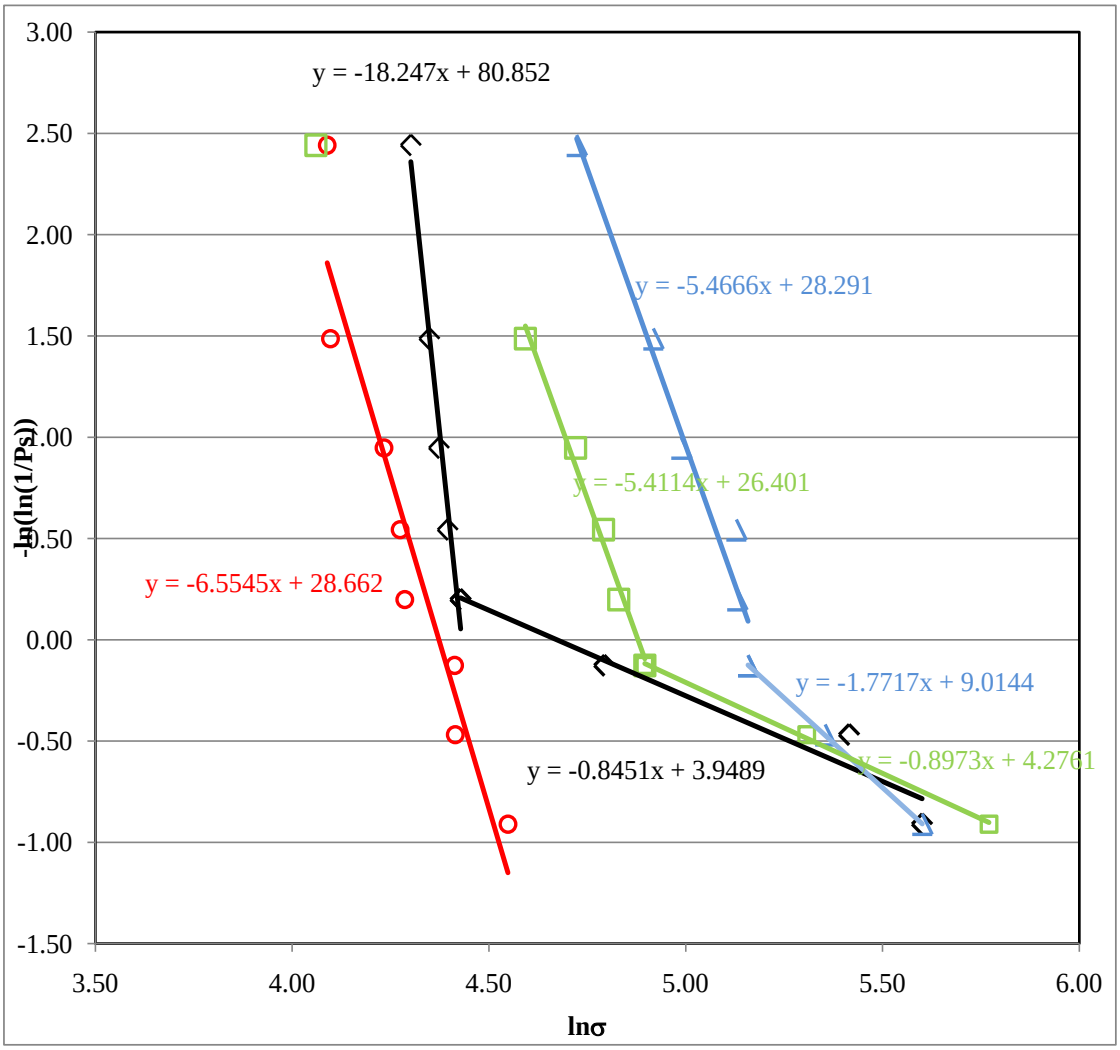

Figure 3.14 Weibull plot for SCZ at room teemrature (black open diamonds), 400 ^{o}C (blue open triangles), 600 ^{o}C (red open circles) and 800 ^{o}C (green open squares)

Table 3.9 Results of Weibull analysis

	Region I		Region II	
Temperature	Weibull modulus, m	Weibull strength, σ_0	Weibull modulus, m	Weibull strength, σ_0
^{o}C		MPa		MPa
25	18.24	84.16	0.85	104.14
400	5.46	177.92	1.77	162.82
600	6.56	79.24	-	-
800	5.41	131.64	0.90	117.58

4. DISCUSSION

Results of microstructural analysis indicate that relatively uniform grain size structure with the average grain size of around 4 μm can be obtained by sintering SCZ powders at 1500 ^{0}C. This result is in good agreement with previously published data [125]. The chemical composition of the sintered samples was found to be relatively homogeneous (**Table 3.2**) with some areas where amount of Sc is significantly lower (1.155 – 3.156 at%) than average value. Previous work by Yarmolonko et al.[125] suggested that in DKKK SZC powders small amount of rhombohedral phase can be present at temperatures below 400 ^{0}C. They showed that the reversible and slow cubic to rhombohedral and rhombohedral to cubic phase transitions occurs at 300-500 ^{0}C upon heating and cooling of $Sc_{0.1}Ce_{0.01}ZrO_2$ ceramics. However, regardless the presence of Sc deficient areas in sinter samples, only cubic fracture was detected by XRD in the present study.

Results of Vickers indentation testing are in good agreement with previously reported results for the materials with similar compositing [126]. Vickers hardens of around 12.5 measured at higher loads is close to previously published value of 12.7 ± 0.5 [126]. It is worth noting here that SCZ exhibit decrease in the hardness with increasing indentation load that is typical behavior of ceramic materials. The indentation fracture toughness determined in this study using Niihara et al.'s and Lankford's method are significantly higher that those determined using Lawn's and Anstis's method, **Table 3.4**. The lower values are close to previously publish data for SCZ ceramic obtained using Single Edge V Notch Beam (SEVNB) technique. More work is needed to understand such a large deference in fracture toughness calculated using different methods.

Figure 3.9 shows that instantaneous coefficient thermal expansion increases with increasing temperature above 400 ^{0}C. The possible reason for increase in CTE is loss of oxygen at higher temperatures in reducing environment [127, 128] that can result in chemical expansion. This process is fully reversible and was intensively studied for another cubic oxide, namely CeO_2. Thermo-chemical expansion of pure and rare-earth

doped CeO_2 has been well studied since it was reported that CeO_2 exhibits significant expansion when exposed to low p_{O2} [129]. Mogensen et al. [129-131] determined CTE of pure and Pr, Gd, Ca, Sm, Gd, La, and Ca doped CeO_2 as a function of temperature and p_{O2} by dilatometry and found that as the degree of doping with two- and three-valent cations is higher, the relative expansion associated with the reduction is smaller. They concluded that chemical expansion is the result of an increase in the ionic radius as Ce^{4+} reduces to Ce^{3+} in order to keep electroneutrality of the crystal during the formation of oxygen vacancies at low p_{O2} and high temperatures. Thermo-chemical expansion of pure and Gd, Y and Sm [132, 133] and Pr [134] was further studied by XRD under various p_{O2} as a function of temperature. Wang et al. [132, 133, 135] demonstrated that the temperature at which significant lattice expansion starts is lower at lower p_{O2}'s. They also showed that a change in the slope of the plot of lattice constant vs. amount of oxide ion vacancies (or non-stoichiometry) occurs at lower vacancy concretions at higher temperatures, and they suggested that the change in the slope can be related to the defect clustering or ordering due to defect association. There is significantly less work published on the effect of oxygen vacancies formation in reducing environment on thermal expansion of fully stabilized ZrO_2. Zhou et al.[136] recently showed that the chemical expansion of yttria stabilized zirconia (YSZ) at 800 ^{0}C and p_{O2}=0.2-10^{-18} atm is insignificant comparable to that of gadolinia doped ceria (GDC) while the YSZ-GDC solid solutions show chemical expansion up to an order of magnitude higher than the pure YSZ and GDC. Thus we can speculate that in examined system namely SCZ thermo-chemical expansion due to change in ionic valence and radii is possible explanation for observed increase in CTE at temperatures above 400 ^{0}C. Another possible reason for observed change in CTW with increasing temperature could be order-disorder transformation. Gibson et al. [137] studied 8 mol% YSZ by neuron diffraction in 25-1000 ^{0}C temperature range in air and found a deviation in the lattice parameter vs. temperature plot at around 650 ^{0}C as indicative of a second-order transition, i.e. order-disorder transformation of vacancy-cation complexes, or clusters.

One of the most intriguing results in this study is non linear change of elastic moduli with temperature, with significant decrease in modulus in 300-600 ^{0}C temperature range, **Figure 3.10**, that corresponds to the temperature range of the frequency dependent loss modulus maxima, **Figure 3.11**. Numerous studies show that the elastic moduli of the fluorite oxide ceramics such as zirconia doped with yttria [138-148], ceria [149], titania [147], and calcia [139, 142] decrease non-linearly with temperature with a significant drop in elastic moduli at temperatures that correspond to the maximum in mechanical damping, i.e. mechanical loss or internal friction Q^{-1}[150] (Q^{-1}=tanφ=E"/E', where φ is loss angle, E' and E" are real and imaginary part of elastic modulus, respectively). It was shown that some of the peaks in the mechanical loss spectra can be related to the anelastic relaxation of elastic (and dielectric) dipoles by jumping of the oxygen vacancy around the dopant. **Figure 4.1** shows mechanical loss spectra for ZrO_2-Y_2O_3 where the peak at lower temperatures for 3, 10 and 12% Y_2O_3 is associated with anelastic relaxation of the $(Y'_{Zr}V''_O)^{\cdot}$ dipole while the peak at higher temperatures and higher level of doping is caused by anelastic relaxation of the $(2Y'_{Zr}V''_O)^{x}$ dipole [139]. For of CeO_2 doped with Mg, Ca, St, Ba, Ce [151] and Sc [135, 152] , the magnitude of internal friction peaks that correspond to anelastic relaxation of vacancy-dopant pair decreases as the radius of dopant ion decreases, i.e. as association enthalpy of the vacancy-dopant pair decreases too.

Here we show for the first time that SCZ has a large frequency dependent relaxation peak, shown in **Figure 3.11**, that is like in the case of YSZ and other doped zirconia and ceria based ceramics most likely caused by anelastic relaxation of oxygen vacancies or vacancy-doping cation clusters. However, the nature of the small hump in the mechanical loss spectra at around 100 ^{0}C, shown in **Figure 3.11,** is still unclear and more work is needed to understand the physical origin of that peak. Another possible mechanism for observed significant drop in elastic moduli in 300-600 ^{0}C temperature range, namely rhombohedral to cubic phase transition has been recently proposed [126] However, since no rhombohedral phase was detected in examined samples and since no abrupt change in CTE that is typical for rhombohedral to cubic first order phase

transition was observed, this mechanism is less likely the reason for observed significant drop in elastic moduli in 300-600 ^{0}C temperature range.

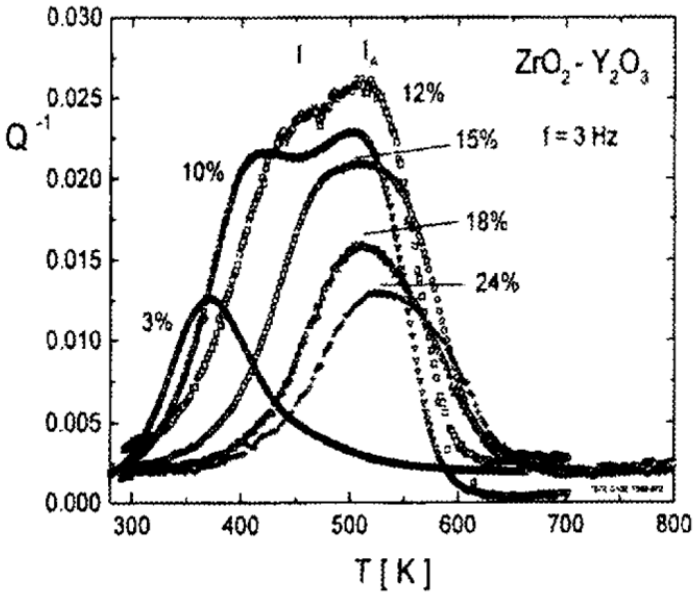

Figure 4.1 Mechanical loss spectra Q^{-1} vs. Temperature in ZrO_2-Y_2O_3. Torsional oscillations, frequency f=3 Hz [139]

Flexural strength reported here is lower than previously reported values for the material with same composition [126] for the reasons that are not clear at this point. However, sigmoid change of flexural strength with temperature, **Figure 3.13**, with the minimum strength at around 600 ^{0}C has also been reported before [126]. Non-linear decrease in strength with temperature can be traced back to the changes in elastic moduli that are caused predominately by change in oxygen vacancy concentration, their association with dopant and/or ordering. Since fracture toughness (K_{IC}) of a brittle solid can be expressed as [150].

$$K_{IC} = \sqrt{\frac{EG_c}{1-\nu^2}} \quad \text{.....(4.1)}$$

where E is Young's modulus, ν is Poisson ration and G_{IC} is the energy required to generate unit area of the crack, it should also depends on oxygen vacancy concentration

in a similar way to the elastic modulus. In addition G_{IC} is also altered by the presence of point defects because anelasticity at the crack tip causes energy dissipation and thus [150]:

$$\Delta G_{IC} = 4\pi r_{tip} W_{stored} \Delta Q^{-1} \quad \text{.....(4.2)}$$

where r_{tip} is the radius of the volume where dissipation takes place during crack propagation, and W_{stored} is maximum stored elastic energy.

Eqs. 4.1 and 4.2 show how fracture toughness can be affected by the presence of point defects. However, as fracture toughness of the brittle solid changes with defect concretion, the strength should also change according to Griffith's criterion:

$$\sigma_f = K_{IC}/Y\sqrt{c} \quad \text{.....(4.3)}$$

where σ_f, Y and c are fracture stress, geometrical factor and critical defect size, respectively. However, vacancy concentration dependence of fracture strength should be the same as that of the fracture toughness, only if the size or distribution of the critical defects does not change with reduction.

Another indirect evidence that cation-vacancy relaxation is responsible for observed minimum in flexural strength at 600 ^{0}C is low standard deviation at that temperature or relatively high Weibull modulus. This indicates very narrow distribution of the measured value of flexural strength for large number of samples. Narrow distribution of flexural strength in ceramics usually indicates that some mechanism, such as cation-vacancy relaxation, that dissipates mechanical energy at the tip of the defect with critical size is operative at specific temperature.

5. FUTURE WORK

From the results presented in this study it is very clear that properties of SCZ makes it very promising material for many applications. Despite the many challenges, SCZ have been proposed for a number of applications, such as thermal barrier coating in gas turbines, fuel cell material, oxygen sensor, catalytic membrane reactors, batteries, automobiles, power generation, electrical vehicle propulsion, solar or wind conversion to electrical energy. As researchers seek to bring these creative ideas to a reality, additional experimental investigation mechanical properties of SCZ electrolyte material for intermediate temperature SOFCs is required in order to make reliable and durable components from SZC. Additional efforts toward improving phase transition are needed and better understanding on how interaction of oxygen vacancies with doping cations, their clustering and relaxation affects mechanical properties of SCZ at elevated temperatures. In addition, in all the abovementioned applications, oxide ceramics are exposed during service to high temperatures, mechanical stresses, and various oxygen partial pressures (as well as oxygen potential gradients). These conditions lead to the formation of point defects -mainly oxygen vacancies- and non-stoichiometry. In fact, most SCZ is more likely to be non-stoichiometric then stoichiometric when exposed to real operating conditions. Thus, better fundamental understanding of how oxygen vacancies affect mechanical properties at elevated temperatures is needed.

6. CONCLUSIONS

In the present study, the instantaneous CTE, elastic moduli, loss modulus, hardness, fracture toughness, and flexural strength of $Sc_{0.1}Ce_{0.01}Zr_{0.89}O_2$ (SCZ) are studied as a function of temperature. It was found that:

- The SCZ samples performed at room temperature have a cubic structure as revealed by XRD, with the average grain size of 4 μm. WDS and EDS analysis also reviled that Zr, Sc, Ce, Hf and Ti relatively homogeneously distributed in the structure.
- Instantaneous coefficient of thermal expansion is $8.726x10^{-6}$ $1/^oC$ in the in 25-400 ^oC temperature range, and increases monotonically with temperature above 400 ^oC to $1.16x10^{-5}$ at 890 ^0C. The increase in CTE is attributed to thermo-chemical expansion due to increase in oxygen vacancy concentration.
- Room temperature hardens decreases with indentation load to 12.5 GPa at loads of 1000 g, while indentation fracture toughness varies from 2.25 to 4.29 $MPam^{1/2}$ depending on the methodology that was used to calculate fracture toughness from the length of the median corner cracks.
- Elastic moduli, namely Young's and shear modulus, decreases with temperature in non-linear manner, with significant drop in the 300-600 ^oC temperature range; the same temperature range in which frequency dependant peaks in loss modulus vs. temperature plots can be observed. The high loss modulus and significant drop in elastic moduli in that temperature regime is attributed to the relaxation of doping cation – oxygen vacancies clusters.
- Flexural strength change with temperature is sigmoidal curve, with the minimum strength at around 600 ^oC. Non-linear decrease in strength with temperature can be traced back to the changes in elastic moduli that are caused predominately by relaxation of oxygen vacancies.

REFERENCES

[1] M.A.J. Cropper, Journal of Power Sources 131 (2004) 57-61.

[2] N.Q. Minh, Journal of American Ceramic Society 76(3) (1993) 563-588.

[3] N.Q. Minh, Solid State Ionics 174 (2004) 271-277.

[4] P. Singh, and N.Q. Minh, International Journal of Application Ceramic Technology 1(1) (2004) 5-15.

[5] S.C. Singhal, Solid State Ionics 152-153(405) (2003) 405-410.

[6] M.C. Williams, Fuel Cells 1(2) (2001) 87-91.

[7] O. Yamamoto, Electrochimica Acta 45 (2000) 2423.

[8] T.P. Chen, J.D. Wright, and K. Krist, in: SOFC V, eds. U. Stimming, S.C. Singhal, H. Tagawa, and W. Lehnert (The Electrochemical Society, Pennington, NJ 97-40, 1997) 69.

[9] B.C.H. Steele, Journal of Material Science 36 (2001) 1053.

[10] P. Holtappels, F.W. Poulsen, and M. Mogensen, Solid State Ionics 135 **(**2000) 675.

[11] H.L. Tuller, in: Oxygen Ion and Mixed Conductors and Their Technological Applications, eds. H.L. Tuller, J. Schoonman, and I. Riess (Kluwer (NATO ASI series), Dordrecht, 2000) 245.

[12] N.Q. Minh, and T. Takahashi, Science and Technology of Ceramic Fuel Cells (1995).

[13] Franklin H. Holcomb, Solid Oxide Fuel Cell (SOFC), http://www.fctec.com/fctec_types_sofc.asp., 7/28/2008.

[14] H. Yamamura, N. Utsunomiya, T. Mori, and T. Atake, Solid State Ionics 107 (1998) 185.

[15] S.P.S. Badwal, F.T. Ciacchi, S. Rajendran, and J. Drennan, Solid State Ionics 109 (1998) (167).

[16] S. Terauchi, H. Takizawa, T. Endo, S. Uchida, T. Terui, and M. Shimada, Materials Letters 23 (1995) 273.

[17] Y. Arachi, T. Asai, O. Yamamoto, Y. Takeda, N. Imanishi, K. Kawate, and C. Tamakoshi, Journal of Electrochemical Society 148(5) (2001) A 520-3.

[18] R. Chiba, F. Yoshinura, T. Yamaki, T. Ishii, T. Yonezawa, and K. Endou, Solid State Ionics 104(3,4) (1997) 259-266.

[19] Anuja Nagle, Solid Oxide Fuel Cell, http://www.ika.rwth-aachen.de/r2h/index.php/Solid_Oxide_Fuel_Cell, 7/28/2008.

[20] K. Kendall, International Materials Reviews 50 (2005) 267.

[21] Holtapples P, Vogt U, Graule T, Advanced Engineering Materials 7 (2005) 292.

[22] Radovic M, and Lara-Curzio E, Acta Materialia 52 (2004) 5747.

[23] M. Taneja, Evaluation of Thermal Stresses in Planar Solid Oxide Fuel Cells as a Function of Thermo Mechanical Properties in Component Materials, Mechanical Engineering, Texas A&M, College Station (2008).

[24] Lin CK, Chen T, Chyou YP, and Chiang LK, Journal of Power Sources 164 (2007) 38.
[25] Laurencin J, Delette G, Lefebvre-Joud F, and Dupeux M, Journal of the European Ceramic Society 28 (2008) 1857.
[26] Atkinson A SA, and Webb S, Solid State Ionics 134 (2000) 59.
[27] Yakabe H, Baba Y, Sakurai T, and Yoshitaka Y, Journal of Power Sources 135 (2004).
[28] Fischer W, Malzebender J, Blass G, and Steinbrech RW, Journal of Power Sources 150 (2005) 73.
[29] Atkinson A, and Selcuk A., Acta Materialia 47 (1999) 867.
[30] Malzbender J, Wakui T, and Steinbrechl R, Fuel Cells 2 (2006) 123.
[31] Atkinson A, and Ramos T, Solid State Ionics 129 (2000) 259.
[32] Swaminathan N, and J. Qu, Fuel Cells 6 (2007) 453.
[33] Krishnamurthy R, and Sheldon B, Acta Materialia 52 (2004) 1807.
[34] Barbashov V, and Komysa Y, Physics of Solid State 47 (2005) 238.
[35] Pannikkat AK, and Raj R, Acta Materialia 47 (1999) 3423.
[36] Larche F, and Cahn J, Acta Materialia 33 (1985) 331.
[37] Durham W, and Schmalzried H, Berichte der Busen-Gesellschaft - Physilkalishe Chemie 91 (1987) 556.
[38] A.R. Allnatt, and A.B. Lidiard, Atomic Transport in Solids (Cambridge University Press, Cambridge, 1993) 50.
[39] T. Ishii, Solid State Ionics 78 (1995) 333.
[40] K. Nomura, Y. Mizutani, M. Kawai, Y. Nakamura, and O. Yamamoto, Solid State Ionics 132 (2000) 235-239.
[41] T.Y. Tien, Journal of American Ceramic Society 47 (1964) 430.
[42] D.W. Strickler, and W.G. Carlson, Journal of American Ceramics Society 48 (1965) 286.
[43] S.P.S. Badwal, and J. Drennan, Journal of Material Science 22 (1987) 3231.
[44] H.L. Tuller, Electrochimica Acta 48 (2003) 2879-2887.
[45] M. Filal, P.C. Mokchah, M.C. Chateau, and J.L. Carpentier, Solid State Ionics 80 **(**1995) 27.
[46] Y. Suzuki, and T. Takahashi, Journal of Chemical Society Japan 11 (1977) 1610.
[47] N.H. Andersen, K. Claussen, M.A. Hackett, W. Hayes, M.T. Hutchings, J.E. Macdonald, and R. Osborn, in: Transport-Structure Relations in: Fast Ion and Mixed Conductors, eds. N.H. Andersen, F.W. Poulsen, K. Clausen, S. Skaarup, and O.T. Sorensen, Riso National Laboratory (Roskilde, Denmark 1985) 279.
[48] J.R. Nicholls, and K.J. Lawson, Surface and Coatings Technology 151-152 (2002) 383-391.
[49] J.A. Kilner, and B.C.H. Steele, in: Nonstoichiometric Oxides, ed. O.T. Sorensen (Academia Press, New York 1981) 233.
[50] A.S. Nowick, in: Diffusion in Crystalline Solids, eds. G.E. Murch, and A.S. Nowick (Academia Press, New York 1984) 143.
[51] M. Weller, Journal of Materials Education 17 (1995) 1.

[52] H.M. Wiedenmann, G. Hotzel, H. Neumann, J. Riegel, and H. Weyl, in: Advances in Ceramics, ed. H. Schaumburg (Sensoranwendungen, B.G. Teubner, Stuttgart 1995) 371-397.
[53] S.P.S. Badwal, Solid State Ionics 52 (1992) 23.
[54] T. Masaki, Journal of American Ceramic Society 69 (1986) 638.
[55] A. Atkinson, and A. Selcuk, Solid State Ionics 134 (2000) 59.
[56] N. Vaidehi, R. Akila, A.K. Shukla, and K.T. Jacob, Materials Research Bulletin 21 (1986) 909.
[57] P. Chowdary, V.A. Tare, and J.B. Wagner Jr, Journal of Electrochemical Society 132 (1985) 123.
[58] S. Pack, in: Proceedings Electrical Conductivity of HgI_2 Containing Al_2O_3 Particles (Electrochemical Society Meeting, Los Angeles, October 1979).
[59] A.H. Heuer, Journal of American Ceramic Society 70 (1989) 689-98.
[60] J. Riegel, H. Neumann, and H.M. Wiedenmann, Solid State Ionics 152-153 (2002) 783.
[61] J.B. Wagner, in: Transport in Nonstoichiometric Compounds, eds. G. Simkowich, and V.S. Stubican (Plenum Press, New York 1985) 3.
[62] M. Miyayama, N. Yanagida, and A. Asada, American Ceramic Society Bulletin. 64 (1985) 660.
[63] I.R. Gibson, G.P. Dransfield, and J.T.S. Irvine, Journal of Materials Science 33 (1998) 4297.
[64] A.J. Feighery, and J.T.S. Irvine, Solid State Ionics 121 (1999) 209.
[65] M. Mori, T. Abe, H. Itoh, O. Yamamoto, Y. Takeda, and T. Kawahara, Solid State Ionics 74 (1994) 157.
[66] X.Q. Liu, and X.M. Chen, Journal of American Ceramic Society 88 (2005) 456.
[67] X.Q. Liu, and X.M. Chen, Ceramics International 30 (2004) 2269.
[68] H. Ruf, and A.G. Evans, Journal of American Ceramic Society 66 (1982) 328.
[69] O. Yamamoto, Y. Arati, Y. Takeda, N. Imanishi, Y. Mizutani, M. Kawai, and Y. Nakamura, Solid State Ionics 124 (1995) 137-142.
[70] A.C. Muller, A. Weber, D. Herbstritt, and E. Ivers-Tiffee, in: Electrochemical Society Proceedings on SOFC VII, eds. S.C. Singhal, and H. Yokokawa (Pennington, NJ) 16 (2001) 952.
[71] J.M. Dixon, L.D. Lagrange, U. Merten, C.F. Miller, and T.J. Porter II, Journal of Electrochemical Society 110 (1963) 276.
[72] S.P.S. Badwal, F.T. Ciacchi, and D. Milosevic, Solid State Ionics 91 (2001) 136-137.
[73] V. V. Kharton, F.M. Figueiredo, L. Navarro, E.N. Naumovich, A.V. Kovalevsky, A.A. Yaremchenko, A.P. Viskup, A. Carneiro, F.M.B. Marques, and J.R. Frade, Journal of Materials Science 36 (2001) 1105.
[74] J.W. Stevenson, K. Hasinska, N.L. Canfield, and T.R. Armstrong, Journal of Electrochemical Society 147 (2000) 3213.
[75] A.A. Yaremchenko, V.V. Kharton, E.N. Naumovich, and F.M.B. Marques, Journal of Electroceramics 4 (2000) 235.
[76] S.A. Kramer, and H.L. Tuller, Solid State Ionics 82 (1995) 15.

[77] H. Arikawa, H. Nishiguchi, T. Ishihara, and Y. Takita, Solid State Ionics 31 (2000) 136-137.
[78] A.A. Yaremchenko, M. Avdeev, V.V. Kharton, A.V. Kovalevsky, E.N. Naumovich, and F.M.B. Marques, Materials Chemistry and Physics 77 (2002) 552.
[79] V.V. Kharton, F.M.B. Marques, and A.A. Atkinson, Solid State Ionics 174 (2004) 135.
[80] S.P.S. Badwal, and J. Drennan, Materials Science Forum 16 (1992) 237.
[81] C. Haering, A. Roosen, H. Schichl, and M. Schnoller, Solid State Ionics 176 **(**2005) 261.
[82] C. Haering, A. Roosen, and H. Schichl, Solid State Ionics 176 (2005) 253.
[83] T.H. Etsell, and S.N. Flengas, Chemical Reviews 70 (1970) 399.
[84] D.W. Stricker, and W.G. Carlson, Journal of American Ceramic Society 48 (1965) 286.
[85] C. Haering, A. Roosen, H. Schichl, and M. Schnoller, Solid State Ionics 176(3-4) (2005) 261-8.
[86] F.M. Spiridonov, L.N. Popova, and R.Y. Popil'skii, Journal of Solid State Chem. 2 (1970) 430.
[87] Z.S. Volchenkova, and V.M. Nedopekin, Inorganic Materials 10 (1974) 1562.
[88] T. Ishii, T. Iwata, and Y. Tajima, Solid State Ionics 57 (1992) 153.
[89] O. Yamamoto, Y. Arati, Y. Takeda, N. Imanishi, Y. Mizutani, M. Kawai, and Y. Nakamura, Solid State Ionics 78 (1994) 158.
[90] O. Yamamoto, Y. Arati, Y. Takeda, N. Imanishi, Y. Mizutani, M. Kawai, and Y. Nakamura, Solid State Ionics 79 (1995) 137-42.
[91] T.I. Politova, and J.T.S. Irvine, Solid State Ionics 168 (2004) 153.
[92] T. Ishii, T. Iwata, and Y. Tajima, in: Proc. 3rd Int. Symp. on SOFC 93-4 (1993) 59.
[93] D.S. Lee, W.S. Kim, S.H. Choi, J. Kim, H.W. Lee, and J.H. Lee, Solid State Ionics 176(9-10) (2005) 33-39.
[94] Z. Wang, M. Cheng, Z. Bi, Y.Dong, H. Zhang, J. Zhang, Z. Feng, and C. Li, Matterials Letters 59(19-20) (2005) 2579-2582.
[95] S. Sarat, N. Sammes, and A. Smirnova, Journal of Power Sources 160(2) (2006) 892-896.
[96] M. Hirano, T. Oda, K. Ukai, and Y. Mizutani, Journal of American Ceramic Society 85(5) (2002) 1336-8.
[97] M. Hirano, T. Oda, K. Ukai, and Y. Mizutani, Solid State Ionics 158(3-4) (2003) 215-23.
[98] J. Kondoh, Y. Tomii, and K. Kawachi, Journal of American Ceramic Society 86(12) (2003) 2093-102.
[99] T.I. Politova, and J.T.S. Irvine, Solid State Ionics 168(1-2) (2004) 153-65.
[100] D.S. Lee, W.S. Kim, S.H. Choi, J. Kim, H.W. Lee, and J.H. Lee, Solid State Ionics 176(1-2) (2005) 33-9.
[101] Z.G. Lv, P. Yao, R.S. Guo, and F.V. Dai, Materials Science and Engineering, A, A458(1-2) (2007) 355-360.

[102] M. de Ridder, R.G. van Welzenis, H.H. Brongersma, and U. Kreissig, Solid State Ionics 158(1-2) (2003) 67-77.
[103] S.P.S. Badwal, Journal of Materials Science Letters 22(11) (1987) 4125-4132.
[104] F.M. Spiridonov, L.N. Popova, and R.Y. Popil'skii, Journal of Solid State Chemistry 2(3) (1970) 430-438.
[105] D.J. Green, R.H.J. Hannink, and M.V. Swain, Transformation Toughening of Ceramics (CRC Press, Boca Raton, FL, 1989).
[106] O. Yamamoto, A. Yoshinori, Y. Takeda, I. Nobuyuki, Y. Mizutani, K. Masayuki, and Y. Nakamura, Solid State Ionics 79 (1995) 137.
[107] Y. Mizutani, K. Hisada, K. Ukai, H. Sumi, M. Yokoyama, Y. Nakamura, and O. Yamamoto, Journal of Alloys Compound 408-412 (2006) 518.
[108] R.H.J. Hannink, P.M. Kelly, and B.C. Muddle, Journal of American Ceramic Society 83 (2000) 461.
[109] D.J. Green, R.H.J. Hannink, and M.V. Swain, Transformation Toughening of Ceramics (CRC Press, Boca Raton, FL, 1989).
[110] Y. Mizutani, K. Hisada, K. Ukai, H. Sumi, M. Yokoyama, Y. Nakamura, and O. Yamamoto, Journal of Alloys Compound (2006) 518.
[111] M. Hirano, M. Inagaki, Y. Mizutani, N. Kazuhiro, K. Masayuki, and N. Yasuhisa, Solid State Ionics 133 (2000) 1.
[112] M. Hirano, S. Watanabe, E. Kato, Y. Mizutani, M. Kawai, and Y. Nakamura, Solid State Ionics 111 (1998) 161.
[113] M. Shimada, and H. Takizawa, in: Ceramics in Charting the Future, ed. P. Vincenzini (Techna Srl, Faenza 1994) 2599-2604.
[114] R. Rosten, M. Koski, and E. Koppana, Journal of Undergraduate Materials Research 2 (2006) 38-41.
[115] T. Yamamoto, H. Kitaura, Y. Kodera, T. Ishii, M. Ohyanagi, and Z.A. Munir, Journal of American Ceramic Society 87 (2004) 1436.
[116] R. Guillemette, Electron Microprobe Laboratory, http://geoweb.tamu.edu/RResearch/probe/Probe_WebPage.html., 10/13/2008.
[117] S.J. Garrett, Introduction to Surface Analysis, http://www.cem.msu.edu/~cem924sg/index.html., 4/3/2009.
[118] K. Niihara, R. Morena, and D.P.H. Hasselman, Journal of Material Science Letters 1 (1982) 13.
[119] J. Lankford, Journal of Material Science Letters 1 (1982) 493.
[120] B.R. Lawn, A.G. Evans, and D.B. Marshall, Journal of American Ceramic Society 63(9-10) (1980) 574.
[121] G.R. Anstis, P. Chantikul, B.R. Lawn and D.B. Marshall, Journal of American Ceramic Society 64 (1981) 533.
[122] V.P. Red'ko, and L.M. Lopato, Inorganic Materials 27(9) (1991) 1609-1614.
[123] L.W. Tai, M.M. Nasrallah, H.U. Anderson, D.M. Sparlin, and S.R. Sehlin, Solid State Ionics 76 (1995) 259-271.
[124] H. Ullmann, N. Trofimenko, F. Tietz, D. Stover, and A. Ahmad-Khanlou, Solid State Ionics 138 (2000) 79-90.

[125] Sergey Yarmolenko, Jag Sankar, Nicholas Bernier, Michael Klimov, Jay Kapat, and Nina Orlovskaya, Journal of Fuel Cell Science and Technology 6 (2009) 021007-1.
[126] S. Lukich, J. Kuebler, and N. Orlovskaya, Mechanical Properties of Sc_2O_3-CeO_2-ZrO_2 Electrolyte Ceramics in Preparation for Submission to Journal of American Ceramic Society in press, 2009.
[127] M.M. Nasrallah, L.W. Tai, H.U. Andersen, D.M. Sparlin, and S.R. Sehlin, Solid State Ionics 76 (1995) 259.
[128] N.T.H. Ullmann, F. Tietz, D. Stover, and A. Ahmad-Khanlou, Solid State Ionics 138 **(**2000) 79.
[129] G. Mogensen, and M. Mogensen, Thermochzmzca Acta 214 (1993) 47.
[130] M. Mogensen, T. Lindegaard, and U. Hansen, Journal of Electrochemical Society 141 (1994) 2122.
[131] M. Mogensen, N. Sammes, and G. Tmpsett, Solid State Ionics 129 (2000) 63.
[132] S. Wang, M. Katsui, T. Hashimoto, and M. Dokiya, Journal of the Electrochemical Society 150 (2003) 952.
[133] S. Wang, E. Okiawa, and T. Hashimoto, Journal of the Electrochemical Society 151 (2004) 46.
[134] S. Rossignol, F. Gerard, D. Mesnard, C. Kappenstein, and D. Duprez, Journal of Materials Chemistry 13 (2003) 3017.
[135] D. Wang, D. Park, J. Griffith, and A. Nowick, Solid State Ionics 2 (1981) 95.
[136] X.-D. Zhou, B. Scarfino, and H.U. Anderson, Solid State Ionics 175 (2004) 19.
[137] I. Gibson, and J. Irvin, Journal of Materials Chemistry 6 (1996) 895.
[138] A. Lakki, R. Herzog, M. Weller, H. Shubert, C. Reetz, O. Gorke, M. Kilo, and G. Borshardt, Journal of the European Ceramic Society 20 (2000) 285.
[139] M. Weller, and A. Lakki, Ber. Bunsenges. Phys. Chem. 101 (1997) 1297.
[140] M. Weller, and H. Shubert, Journal of the American Ceramic Society 69 (1986) 573.
[141] M. Radovic, E. Lara-Curzio, R. Trejo, B. Armstrong, and C. Walls, "Elastic Properties, Equibiaxial Strength and Fracture Toughness of 8mol%YSZ Electrolyte for SOFC" presented at 28th Cocoa Beach Conference on Advanced Ceramics and Composites Ceramics 25 (3) (2003) 287.
[142] Q. Fang, T. Liu, C. Li, X. Wang, and G. Zhang, Key Engineering Materials 319 (2006) 167.
[143] G. Roebben, B. Basu, J. Vleugels, and O. Van der Biest, Journal of European Ceramic Society 23 (2003) 481.
[144] S. Shepel, and B. Drapkin, Journal of Materials Science Letters 17 (1998) 1991.
[145] M. Weller, F. Khelfaouia, M. Kilob, M.A. Taylor, C. Argirusisb, and G. Borchardtb, Solid State Ionics 175 (2004) 329.
[146] M. Weller, B. Damson, and A. Lakki, Journal of Alloys and Compounds 310 (2001) 47.
[147] M. Weller, H. Shubert, and P. Kountouros, in: Science and Technology of Zirconia V, eds. S.P.S. Badwal, M.J. Bennister, and R.H.J. Hannink (Technomic, Lancaster, Basel 1993) 546.

[148] S. Giraud, and J. Canel, Journal of the European Ceramic Society 28 (2008) 77.
[149] M. Ozawa, T. Itcho, and E. Suda, Journal of Alloys and Compounds 373 (2004) 120.
[150] R. Schaller, G. Fantozzi, and G. Gremaud eds., in: Mechanical Spectroscopy Q-1 2001 (Trans Tech Publications Ltd, Zuerich, 2001).
[151] K. Matsushita, Journal of Alloys and Compounds 211 (1994) 374-377.
[152] R. Gerhardtanderson, F. Zamaninoor, A.S. Nowick, C.R.A. Catlow, and A.N. Cormack, Solid State Ionics 9-10 (1983) 931.

VITA

Wendy Lim

Wendy Lim was born in Pontianak, Indonesia. After completing his work at Santu Petrus high school, he went to Austin Community College in Austin, TX. Then he transferred to The University of Texas in Austin, Texas to pursue his study in mechanical engineering. He received his Bachelor of Science degree in mechanical engineering from University of Texas in Austin, Texas in Summer 2005. He entered graduate studies in the Mechanical Engineering program at Texas A&M University in August 2007 and received his Master of Science degree in December 2009. He is a recipient of MSEN and MEEN Scholarship/Fellowship. At Texas A&M University, Wendy works for Dr. Miladin Radovic on materials for Solid Oxide Fuel Cell (SOFC). His email is rievas@gmail.com.

Wendy's address follows:
Texas A&M University
Department of Mechanical Engineering
3123 TAMU
College Station, TX 77843-3123
USA